Frictional properties of rocks recovered form aftershock cloud of the 2014 Orkney earthquake (M5.5), South Africa, by ICDP-DSeis

Yasuo YABE[1]

[1]Affiliation not available

December 10, 2023

Frictional properties of rocks recovered from the aftershock cloud of the 2014 Orkney earthquake (M5.5), South Africa, by the ICDP-DSeis project

Yasuo Yabe[1], Hiroshi Ogasawara[2], Raymond Durrheim[3]

[1] Graduate School of Science, Tohoku University

[2] College of Science and Engineering, Ritsumeikan University

[3] School of Geoscience, The University of Witwatersrand

Corresponding author: Yasuo Yabe (yasuo.yabe.e2@tohoku.ac.jp)

Key Points:

- The frictional properties of rocks recovered from the active aftershock cloud of the M5.5 earthquake were examined in the laboratory.
- The evolution of friction with sliding is key to understanding aftershock activity on a fault where the mainshock rupture was terminated.
- The evolution of the frictional properties is correlated with the development of texture in the sheared gouge layer.

Abstract

To understand the frictional properties of a fault where the rupture propagation of an M5.5 earthquake was terminated, with high aftershock activity, we conducted a series of rotary shear tests with up to 172 mm of sliding using rock samples recovered from the fault by the ICDP-DSeis project. The fault is located in an altered lamprophyre dike that intruded into the Crown Formation, which as an altered basalt. As drilling water temporarily leaked during fault drilling, the tests were conducted under dry (5% RH) and wet (saturated, but without pore pressure) conditions. The friction coefficient (μ) of dry lamprophyre is as high as dry Crown basalt (μ: 0.6–0.8). The frictional behavior of the lamprophyre began with rate-strengthening and evolved into rate-weakening with sliding. The evolution rate depends on the normal stress, reflecting the difference in the maturity of shear texture in the gouge. Wet lamprophyre is considerably weaker (μ: 0.2–0.3) than wet Crown basalt (μ: 0.6–0.8) and shows rate-strengthening independent of the sliding distance. Acoustic emission (AE) activity in the wet lamprophyre gouge increased with increasing sliding distance. The AE activity depends on normal stress. These findings explain the high aftershock activity on the fault that terminated the propagation of mainshock rupture. The normal stress dependence of the evolution rate of the friction behavior of the dry lamprophyre and that of the AE activity of wet lamprophyre may have caused the spatial and size distributions of the aftershocks to reflect the stress distribution along the fault.

Plain Language Summary

Aftershock activity is known to be high in areas surrounding the mainshock rupture. This suggests that the surrounding area is aseismic when the mainshock occurs but evolves into a seismic region. To understand the underlying process of this evolution, the frictional properties of rocks in the aftershock cloud of an M5.5 earthquake recovered by the ICDP-DSeis project were measured through laboratory tests using a rotary shear apparatus. Under dry conditions, the fault properties evolved from aseismic to seismic with increasing sliding distance. When the fault is wet, it is always aseismic, but acoustic emissions that mimic aftershocks are increasingly observed with increasing sliding distance. The evolution depends on the normal stress. Therefore, the size and spatial distribution of the aftershocks reflects the stress state around the fault. Our experimental results thus explains high aftershock activity on the fault which terminates the propagation of mainshock rupture. However, they cannot justify the nucleation of

mainshock on the fault. To explore the nucleation process, new drilling to the mainshock hypocenter is needed.

Index terms

- 8163 Rheology and friction of fault zones (8034)
- 7209 Earthquake dynamics (1242)
- 7215 Earthquake source observations (1240)
- 8004 Dynamics and mechanics of faulting (8118)

Key words

- Active fault drilling
- Rotary shear test
- Acoustic emission (AE) activity associated with the frictional sliding
- Evolutions of frictional properties and AE activity with sliding

1 Introduction

Following an earthquake, aftershocks are most active in the area surrounding the rupture area of the mainshock and expand over time (e.g., Chang & Ide, 2020; Kato & Obara, 2014; Mogi, 1968; Tajima & Kanamori, 1985). The complementary distributions of the mainshock rupture and aftershock activity imply that the area surrounding the mainshock is stable during the propagation of mainshock rupture. With elapsed time and/or accumulated aseismic slip, the area surrounding the mainshock becomes unstable, and aftershocks may nucleate. Understanding the time- and/or slip-dependent evolution of fault behavior is important for investigating the termination processes of earthquakes, predicting aftershock activity, and evaluating hazards induced by aftershocks. It also aids in elucidating the underlying physics of the asperity model and the conditions for the coalescent faulting of asperities to generate a large earthquake, such as the 2011 Tohoku-oki earthquake (Mw9.0).

Drilling into a seismogenic fault provides good opportunities to investigate micro-structures (Bradbury et al., 2011; Bouller et al., 2009; Chester et al., 2013) and to determine its mechanical (Carpenter et al., 2015; Chéry et al., 2004; Fulton et al., 2013; Wu et al., 2007; Yabe et al., 2008; Yabe et al., 2022), chemical (Li et al., 2013; Moore, 2014; Schleicher et al., 2015), and hydrological (Fujimoto et al, 2007; Tanikawa et al., 2013) properties. As these knowledges are fundamental to understand and evaluate hazards induced by earthquakes and to mitigate its risks, fault-zone drilling has been a centerpiece of the International Continental Scientific Drilling Program (ICDP) since its foundation in 1996 (ICDP Science Plan 2020-2030). Numerous attempts, such as the San Andreas Fault Observatory at Depth project (SAFOD, Zoback et al., 2011) and the Taiwan Chelungpu Fault Drilling Project (TCDP, Ma et al., 2006) have been made to drill holes into active faults. However, to the best of our knowledge, none of these wells have reached the seismogenic depths at which regular earthquakes nucleate. In particular, the drilling of the SAFOD project successfully reached a 2.7 km depth from surface and intersected the San Andreas Fault. Moore & Rymer (2007) identified talc from cuttings containing serpentinite in the rotary drilling. The drilling site was in the transition zone between the locked and constant creep areas of the San Andreas Fault. However, as the SAFOD drilling did not reach the main rupture zone of the M~6 repetitive earthquakes or a streak of the stationary microseisms in the basement lithology (P-wave velocity Vp~6 km/s), there was no opportunity to discuss the role of talc where seismic activity is actually occurring. The TCDP drilling intersected with the fault zone of the 1999 Chi-Chi earthquake (M7.7), Taiwan, at a depth of about 1110 m in the Chinsui shale. Kano et al. (2006) detected temperature anomaly of 0.06℃ at the depth of fault intersection and concluded an apparent coefficient of friction was as low as 0.04-0.08. Wu et al. (2007) and Yabe et al. (2008) showed that the stress state along the TCDP hole was significantly perturbed around the fault. However, *Vp* of the Chinsui shale was ~4 km/s (Wu et al., 2007) and aftershock rarely occurred beneath the drilling site (Kim et al., 2010).

The 2014 Orkney earthquake (M5.5) occurred on August 5, 2014 below the Moab Khotsong gold mine near Orkney, approximately 150 km southwest of Johannesburg, South Africa (Figure 1a, Midzi et al., 2015). The mainshock and aftershocks were clearly recorded by surface accelerometers operated by the South African Council for Geoscience (Manzunzu et al., 2017; Midzi et al., 2015) and by in-mine geophones and strainmeters (Ogasawara et al., 2017, 2019). The mainshock was located at a depth of 4.7 km. The aftershocks delineate an approximately 3-km long NNW–SSE-striking planar cloud at depths of 3.5–7 km south of the mainshock hypocenter. The hypocenters were significantly deeper than those of typical mining-induced earthquakes in the mining district near Orkney (2–3 km below the surface; Ogasawara et al., 2017). Furthermore, the focal mechanism solution of the mainshock is strike-slip faulting, wherein one of the nodal planes coincides with the plane delineated by the aftershocks. This is in contrast to normal faulting that is typical for mining-induced earthquakes, but is consistent with the regional stress field associated with the East African rift system (Manzunzu et al., 2017). Therefore, the Orkney earthquake is considered to have occurred in response to a regional tectonic stress field. Mori et al. (2019) inverted seismograms recorded by surface accelerometers and in-mine geophones. They showed that the coseismic slip during the mainshock mostly occurred in two slip patches in the north and below the mainshock hypocenter (red ellipsoids in Figure 1b) and was minor or negligible in the aftershock cloud area. Okubo et al. (2017) back-projected seismograms recorded by surface accelerometers to estimate strong motion generating area (SMGA, blue ellipsoids in Figure 1b) of the mainshock. They identified three SMGAs. One of the three SMGAs coexisted with the northern slip patch and other was just above the slip patch below the mainshock hypocenter. The other SMGA existed above the mainshock hypocenter.

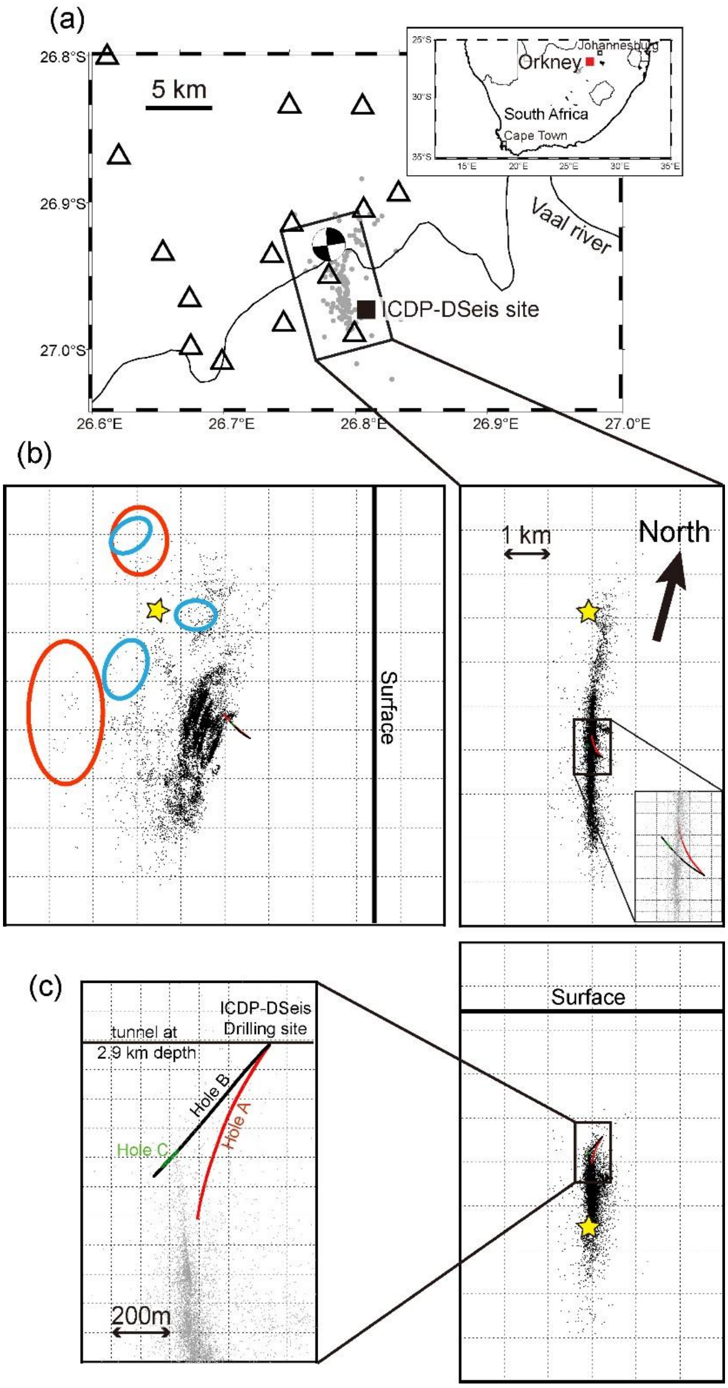

Figure 1. (**a**) Location of the drilling site with epicenters of the mainshock and aftershocks (gray circles) determined by Okubo et al. (2017) using on-surface seismic stations (triangles) operated by the Council for Geoscience. The focal mechanism solution of the mainshock determined by USGS is shown at its epicenter. The red square in inset map indicates location of Orkney. (**b**) Map view and cross-sections of the mainshock hypocenter (yellow star) and aftershocks (black dots) within 1 month after the mainshock located using an in-mine seismic network. The red and blue ellipsoids in the along-strike cross-section indicate the slip patches and SMGAs, respectively. Traces of Holes A, B, and C are also indicated by red, black, and green lines, respectively. Epicenters in the inserted map represent those shallower than 4 km. (**c**) An enlarged cross-section normal to the strike of aftershock distribution (N15W) and drilling traces. We plotted hypocenters within 500 m from the hole collar along the aftershock distribution.

The "ICDP - Drilling into Seismogenic zones of M2–5.5 earthquakes in deep South African gold mines" (ICDP-DSeis) project (Ogasawara et al., 2017, 2019) is an international drilling project operated by researchers from Japan, South Africa, USA, Germany, Switzerland, India, Australia, and Israel with funding and technical support by ICDP. The objectives of this project were to recover rock samples from the aftershock cloud of the Orkney earthquake, elucidate the stress state in and around the aftershock cloud, and explore the deep biosphere. The drilling site for the ICDP-DSeis project was established on a horizontal tunnel at a depth of 2.8 km in the Moab Khotsong mine. Three boreholes, namely, Holes A, B, and C, were drilled toward the aftershock cloud (Figures 1b and c). Drilling commenced in June 2017 and ended in July 2018.

Hole A (drilled length of 817 m) failed to reach the aftershock cloud because of the deviation of the borehole from its planned trajectory, and ran roughly parallel to the cloud. Nisson et al. (2023) and Warr et al. (2022) reported outflows of long-isolated (>1.0–1.2 Ga) and hypersaline (215–246 g/L) brine from a fracture in the Onstott dike intersected by Hole A. Temperature of the hypersaline brine was 55°C and pressure was 10 MPa. Hole B (drilled length of 700 m) intersected a 3-m wide fracture zone into which drilling fluid was lost at a depth of ~610 m below the hole collar (hereafter, positions in the borehole and of the core are downhole distances). Drilling cores were not retrieved, and only fragmented rocks were recovered from this fracture zone (hereafter called the core-loss zone). Except for the core-loss zone, continuous core samples were successfully recovered from Hole B. The core-loss zone coincided spatially with the aftershock cloud, suggesting that it corresponded to the source fault of the Orkney earthquake (Ogasawara et al., 2019). The loss of the drilling fluid implies that the pores in the core-loss zone may be empty. Even when water is present, the pore pressure should be lower than the water head pressure of 5 MPa in the borehole, which is significantly lower than the overburden pressure of 90 MPa. Hole C (drilled length of 96 m) branched out from Hole B at 544 m to collect samples corresponding to the core-loss zone using a triple-tube core barrel. The fault-related samples from Holes B and C are the first to be retrieved from within the aftershock cloud of a natural tectonic earthquake (M > 5) and provide a rare opportunity to improve our understanding of seismogenic processes and the stress state in a seismogenic zone.

Nkosi et al. (2022) and Ogasawara et al. (2019) summarized the post-drilling core logging, downhole logging, and core curation of the ICDP-DSeis project. They found that the source fault occurred in a dike that intruded the Crown Formation of the

Jeppestown Subgroup of the West Rand Group. The Crown Formation comprises Archean flood basalt dated to 2,914 Ma (Armstrong et al., 1991; the Crown Formation in Hole B is hereafter referred to as the Crown Lava, the name used by local mine geologists and rock engineers). Nkosi et al. (2022) reported that the density ρ, porosity φ, P-wave velocity Vp, and S-wave velocity Vs, of the Crown Lava are 2720-2830 kg/m^3, 0.79-1.01%, 5989-6530 m/s, and 3017-3922 m/s, respectively. Those of the dike are ρ = 2880-3090 km/m^3, φ = 0.96-1.02%, Vp = 5399-6743 m/s, and Vs = 3083-4126 m/s. Miyamoto et al. (2022) analyzed the mineralogical and chemical components of the dike hosting the source fault and Crown Lava on both sides of the dike between 530 and 660 m of Hole B. As the dike is characterized by low contents of quartz and feldspar and high contents of amphibole, biotite, talc, and calcite, it is defined as an altered lamprophyre (hereafter, the dike is referred to as Lamprophyre). They also conducted friction tests using a direct shear apparatus under ambient conditions and a normal stress of 40 MPa to measure the friction coefficient and its rate-dependence. The Lamprophyre showed a smaller friction coefficient than the Crown Lava and rate-hardening behavior. These results are consistent with the occurrence of the source fault in the lamprophyre dike and termination of rupture propagation around the ICDP-DSeis holes. However, this contradicts the high aftershock activity around the ICDP-DSeis holes.

In this study, we examined the frictional properties of the Crown Lava and Lamprophyre recovered from Hole B of the ICDP-DSeis project under wider conditions than those of Miyamoto et al. (2022) in terms of the water content and normal stress. We also measured the acoustic emission (AE) activity associated with frictional sliding. The maximum sliding distance was set to 172 mm to evaluate the evolution of the friction properties and AE activity.

2 Methods

2.1 Sample preparation

To investigate the differences in frictional properties between fractured and intact Lamprophyre, as well as those between the Crown Lava and the Lamprophyre, we selected one sample from the Crown Lava on each side of the Lamprophyre, two samples from the intact Lamprophyre, and two samples from the core-loss zone (fractured Lamprophyre, see Figure 6). In particular, the Crown Lava samples of MKB74-1-4 and MKB75-1-1 were collected 2 and 0.3 m east and west, respectively, from the contact between the Crown Lava and Lamprophyre. Samples MKB74-4-6a and MKB74-4-8 were selected from the middle portion of the intact Lamprophyre east of the core-loss zone. The minerals and major elements contained in these samples, as well as the fractured Lamprophyre samples (UFZ and LFZ), are shown in Figure 2. As previously stated, most rock fragments in the core-loss zone were lost during drilling. The recovered rocks were loosely packed into sample tubes. Therefore, the exact depths of the UFZ and LFZ could not be identified, but they were sampled as representative materials from the east and west halves of the core-loss zone, respectively. As the drilling rod was broken during the drilling of the core-loss zone, the steel fragments were mixed into the UFZ and LFZ samples. The steel fragments were removed using a magnet before grinding. As noted by Miyamoto et al. (2022), lamprophyres contain minerals with high magnetic susceptibility, probably magnetite. Some of these minerals might also be removed using this procedure.

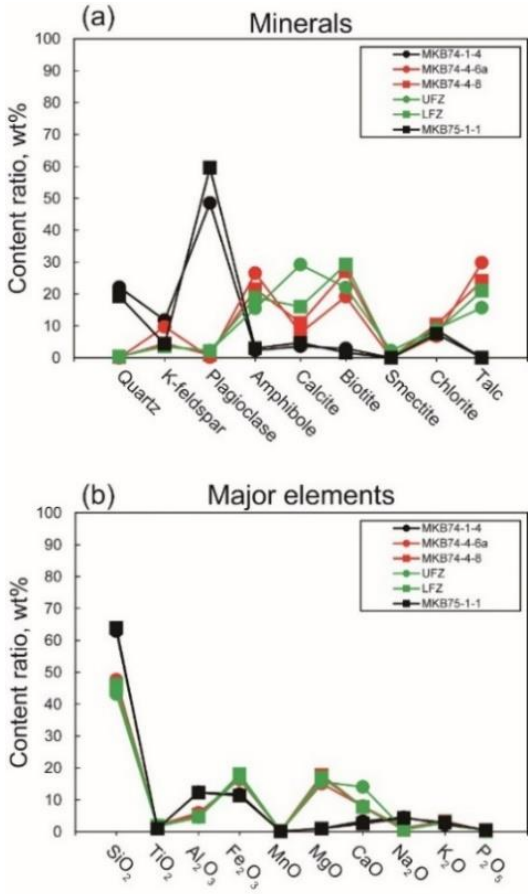

Figure 2. (**a**) Minerals and (**b**) major elements contained in samples measured by Miyamoto et al. (2022). Black, red, and green symbols indicate the Crown Lava, intact Lamprophyre, and fractured Lamprophyre, respectively.

Each sample was ground into a fine-grained powder (gouge). Subsequently, the powder was sieved with a mesh containing openings with a size of 106 μm. One gram of the gouge was weighed out and wrapped in drug packing paper. It was stored in a plastic bag with a dehydration agent (silica gel) to keep the gouge under a dry condition with a relative humidity (RH) of ~5%.

The particle size distributions of the MKB75-1-1 (Crown Lava) and LFZ (fractured Lamprophyre) gouges were measured using laser diffraction (Figure 3). The median particle sizes of MKB75-1-1 and LFZ are 30 and 7.8 µm, respectively. The maximum particle sizes of MKB75-1-1 and LFZ are 246 and 146 µm, respectively, and are larger than the mesh openings of 106 µm. This suggests that the gouges contain ellipsoidal particles. The particle size distribution of MKB75-1-1 has a single peak at ~90 µm. The particle size of LFZ clearly shows bimodal distribution with a primary peak at ~6 µm, which is similar to the median size, and a secondary peak at ~70 µm. The primary peak may reflect the thickness of the platy minerals (biotite and talc).

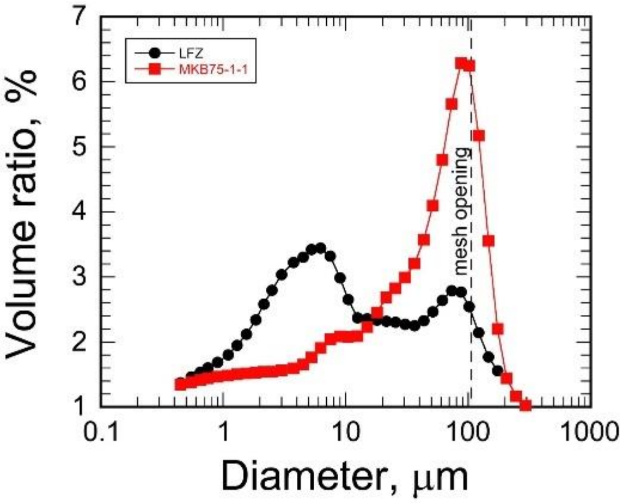

Figure 3. Particle size distributions of the lamprophyre (LFZ, black circles) and Crown Lava (MKB75-1-1, red squares). The vertical dashed line indicates the mesh opening (106 µm) used to sieve gouges. The peak at a diameter of approximately 6 µm of LFZ may correspond to the thickness of platy minerals, such as biotite and talc.

2.2 Experimental procedure

2.2.1 Apparatus

Friction tests were conducted using a rotary shear apparatus (Figure 4a). The normal load was measured using a load cell and kept constant by a computer-based servo-controlled hydraulic system with an accuracy of 1.6% or better. The shear stress was calculated from the torque measured 150 mm from the central axis of the upper forcing block. The normal load and torque were recorded at 10-kHz sampling rate with 24-bit resolution.

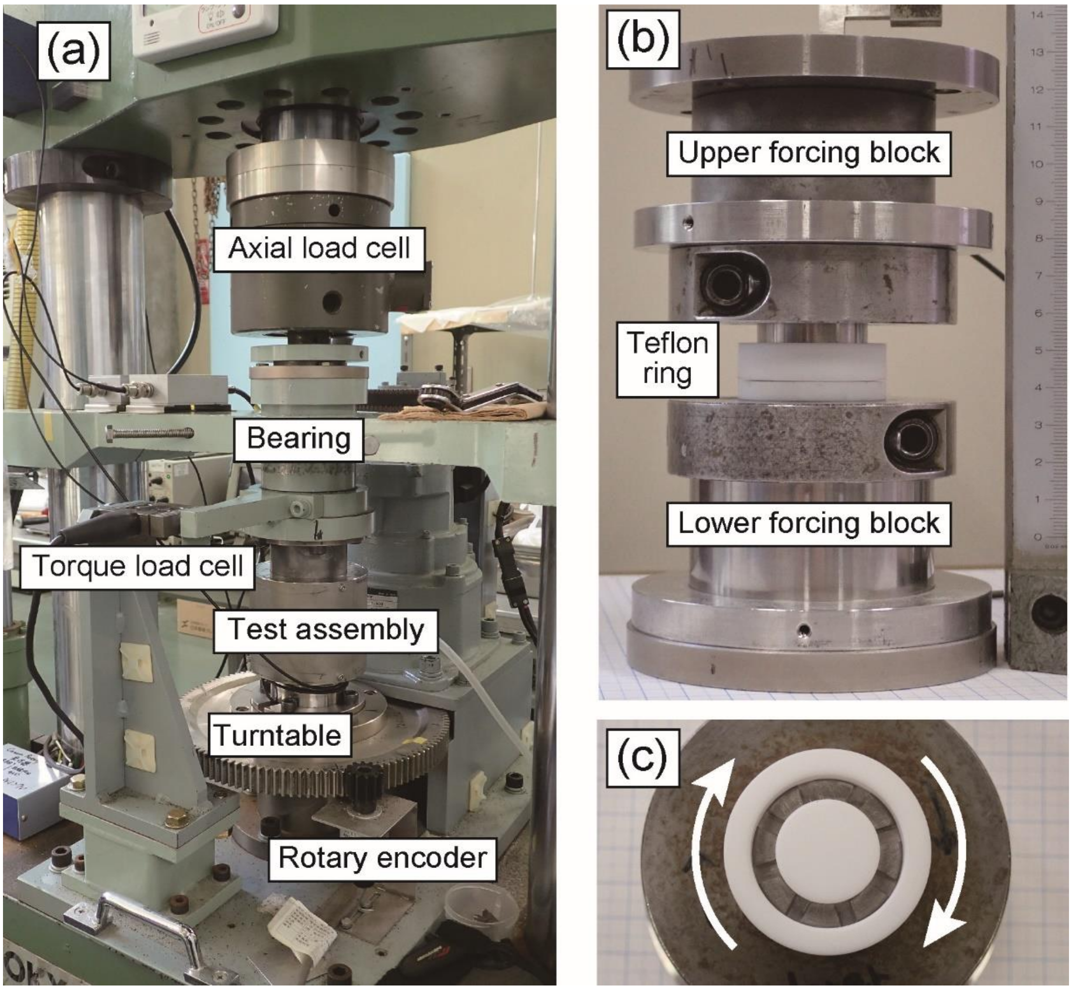

Figure 4. Photos of the (**a**) loading apparatus, (**b**) test assembly without the chamber. The AE sensor is buried in forcing blocks, and (**c**) interface of the lower forcing block. The gouge is confined in an annular interface between the upper and lower forcing blocks by a Teflon ring and plug. White arrows in (c) indicate the rotation direction.

The stroke of the vertical ram that was used to apply a normal load was measured using a linear variable differential transformer (LVDT). The lower forcing block is fixed to the turntable. The turntable was rotated using a pulse motor, the rotation rate of which was controlled based on the prescribed loading sequence. The rotation angle of the turntable was measured using a rotary encoder with a resolution of 810,000 pulses/rotation. The outputs of the rotary encoder and LVDT were recorded at 200 kHz with 16-bit resolution.

The test assembly comprised upper and lower forcing blocks (Figure 4b) and a steel chamber. The forcing blocks were made of stainless steel and had annular interfaces with inner and outer diameters of 20 and 30 mm, respectively. Radial grooves with a width and depth of 3.4 and 1 mm, respectively, were machined on the interface every 45° to suppress boundary slip (Figure 4c).

The gouge layer was sandwiched between the annular interfaces and confined using a Teflon ring and plug. As described below, the additional frictional resistance induced by the Teflon ring and plug was estimated to be less than the fluctuation amplitudes of friction during the test. Therefore, we did not correct for the additional friction. Notably, the chamber did not induce extra friction because there was clearance between the lower forcing block and chamber.

A broadband (0.5–1.2 MHz) AE sensor was installed in each forcing block to observe AE activity. The AE waveforms were amplified by 50 or 60 dB and a 100-kHz high-pass filter was applied. The AE waveforms were then fed to the rectifier, whose decay time was 100 μs, to obtain AE envelopes (Yabe et al., 2003). The AE envelopes were recorded at 100 kHz with 18-bit resolution.

2.2.2 Preparation of the gouge layer

As suggested by the loss of drilling fluid in the core-loss zone, the in-situ aqueous conditions could be dry. Even in the presence of water, the pore pressure was less than 5 MPa. Therefore, the gouge layer was prepared for the dry and wet tests using the following procedure. A Teflon ring and plug were attached to the lower forcing block. The gouge (1.0 g) quickly spread over the annular interface under ambient conditions. The lower forcing block was knocked to achieve a gouge distribution that was as uniform as possible. The upper forcing block and a chamber were installed. The upper forcing block was rotated by hand to ensure uniform gouge thickness. After confirming the parallelism between the interfaces of the upper and lower forcing blocks using a bubble level, the assembled forcing blocks were set to the rotary shear apparatus and pre-conditioned air flowed into the chamber. Although this procedure typically requires a short time (less than 5 min), some moisture can be absorbed by the gouge. To remove the absorbed moisture, dry air, dehydrated to an RH of ~5% by silica gel and an anhydrous calcium sulfate desiccant, was made to flow into the chamber for ~17 h following the assembly setup in the case of the dry test. In the wet test, deionized water was added to the gouge layer before installing the upper forcing block. The assembled forcing blocks were left under room or humid conditions (100% RH) for ~17 h before testing to ensure uniform percolation of water through the gouge. No pore pressure was applied during the wet tests in this study.

2.2.3 Loading procedure

A normal stress σ_n of 5 or 15 MPa was applied. After the pre-compaction of the gouge layer for 1 h, we conducted a sliding-rate step test. The sliding rate and sliding distance were calculated along the reference radius $r_r = \sqrt[3]{({r_o}^3 + {r_i}^3)/2}$, where r_o and r_i are the outer and inner radii of the interface, respectively. The reference radius was defined such that the seismic moment rates released from the inside and outside were equal. For the interface used in this study, r_r was 12.98 mm and a nominal circumference along the reference radius was 81.56 mm. Therefore, the sliding distance corresponding to the resolution of the rotary encoder was approximately 0.10 μm. The sliding rate was changed stepwise between 4.64 and 46.4 μm/s by every 1/3 order of magnitude. When the cumulative sliding distance is small, the frictional properties quickly evolve with sliding (e.g., Marone et al., 1992; Yabe, 2002). The AE activity decreases with increasing cumulative sliding distance (Yabe, 2002). Therefore, the steps were imposed after every 1 mm of sliding up to a sliding distance of 29 mm and subsequently after every 2 mm of sliding up to a sliding distance of 172 mm (Figure S1 in Supporting Information).

After conducting the sliding-rate-step test under a constant normal stress, the normal stress was reduced stepwise under a constant sliding rate of 10 μm/s. As the frictional resistance induced by the Teflon ring and plug acts on the sidewalls of the forcing blocks, it should be independent of the normal stress. Therefore, it can be estimated by extrapolating the steady-state friction to $\sigma_n = 0$ MPa. However, the estimated extra friction varied significantly between the tests, suggesting that the extra friction and cohesion of the gouge were much smaller than the fluctuation amplitudes of friction (typically less than 0.03) during the test.

2.3 Data analysis

2.3.1 Mechanical data

Mechanical data of the normal load, torque, and ram stroke were resampled by averaging for every 0.1 μm of sliding, which was the resolution of the rotary encoder. The normal stress is calculated by dividing the normal load by the nominal area of the annular interface. When shear stress τ was assumed to be uniform over the annular interface, it equilibrated with the torque T as $T = 2\pi\tau \int_{r_i}^{r_o} r^2 dr$. As stated above, the cohesion of the gouge was negligible, and the friction coefficient was defined as the ratio of the shear stress to the normal stress.

The friction coefficient was superimposed by fluctuations as typically observed in the evolution of the friction coefficient of MKB74-4-8-20220824 (Figure S3 in Supporting Information). It is concave at sliding distances of ~40 and ~120 mm and convex at ~80 and ~150 mm. As these intervals of concave and convex parts almost corresponded to the nominal circumference of the interface, this may have been ascribed to the eccentricity of the test assembly. The following function was fitted to the evolution of the friction coefficient for sliding distances of $5 \leq d \leq 165$ mm to estimate the initial friction coefficient μ_i at $d = 0$ and hardening rate μ_h;

$$\mu = \mu_i + \mu_h d + \mu_f \sin\left(\left(d - d_f\right)/d_r\right) \tag{1}$$

where d is the sliding distance in mm, μ_f and d_f represent the amplitude and initial phase, respectively, of the fluctuation of the friction coefficient. Period d_r is fixed to 81.56 mm, and is the sliding distance for one rotation. As the gouge was squeezed out before reaching the final sliding distance (172 mm) in the six tests, equation (1) was not applied to these tests; however, the mean friction coefficient was calculated.

Frictional properties were evaluated by visually fitting the rate- and state-dependent friction (RSF) laws (Dieterich, 1979; Ruina 1983) with two state variables (equations 2 and 3) on the frictional response against the sliding-rate step (Figure 5).

$$\begin{cases} \mu = \mu_0 + a \ln\left(\dfrac{V}{V_0}\right) + b_1 \ln\left(\dfrac{V_0\theta_1}{Dc_1}\right) + b_2 \ln\left(\dfrac{V_0\theta_2}{Dc_2}\right) & (2) \\ \dfrac{d\theta_i}{dt} = -\dfrac{V\theta_i}{Dc_i} \ln\left(\dfrac{V\theta_i}{Dc_i}\right) & (3) \end{cases}$$

where μ and V are the friction coefficient and sliding rate, respectively, and μ_0 and V_0 are their reference values. a, b_i, and Dc_i ($i = 1, 2,\ Dc_2 > Dc_1$) are frictional parameters that characterize the frictional response in the RSF law. θ_i represents the state variables. t is time. The theoretical friction response was calculated by numerically integrating a quasi-static 1-D spring-slider model (equation 4) using the fourth order Runge-Kutta method.

$$k\ (V_l - V) - \frac{d\mu}{dt} - \eta \frac{dV}{dt} = 0 \tag{4}$$

where k is the stiffness of the loading system and V_l is the loading rate. η represents the seismic radiation dumping (Rice, 1993) and was set to 10^{-6}. The stiffness was determined for each sliding-rate step to reproduce the delay in peak friction after the stepwise change in the sliding rate. The sliding rate measured using the rotary encoder was substituted with V_l. The fitting window length was not fixed but was adjusted for each sliding-rate step to ensure that the steady state after the sliding-rate step could be included.

Although the first-order long-term slip hardening and fluctuation in friction can be evaluated by equation (1), the estimation of RSF parameters for individual sliding-rate steps is also affected by higher-order fluctuations. Therefore, higher-order fluctuations were corrected by excluding the linear trend estimated from the friction data immediately before each sliding-rate step.

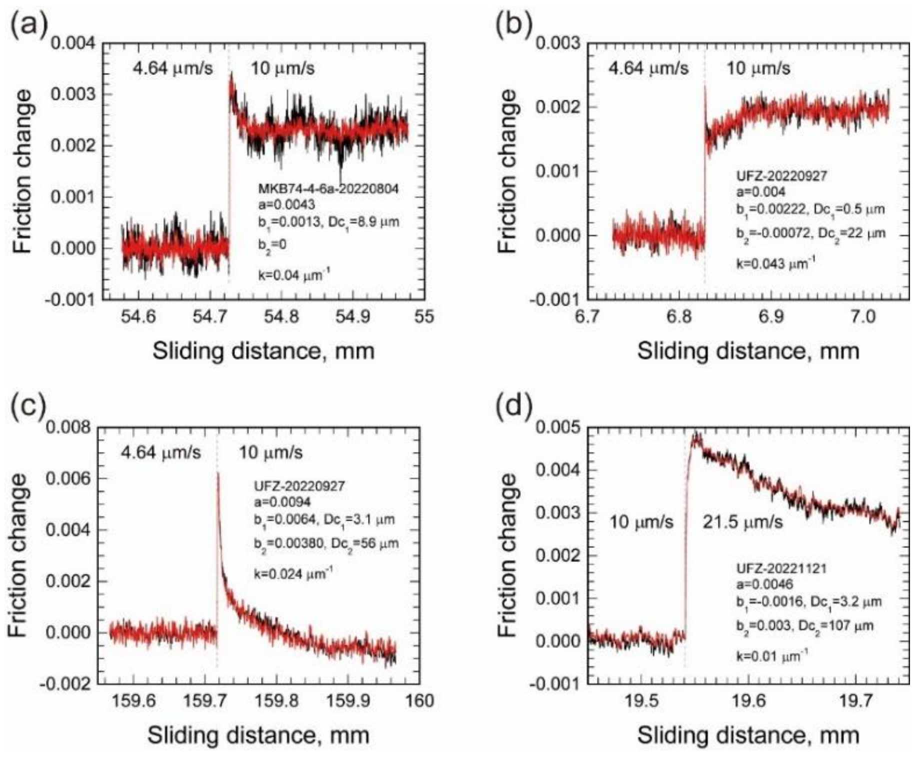

Figure 5. Examples of fitting of equations (2)–(4) (red line) to the data (black line) for the (**a**) dry Crown Lava, (**b**)-(**c**) dry fractured Lamprophyre, and (**d**) wet fractured Lamprophyre. Loading rates before and after the sliding-rate step at the vertical dashed line as well as the estimated RSF parameters are shown. A linear trend and the steady state friction coefficient determined from the data before the sliding-rate step are subtracted. Horizontal axis is the cumulative sliding distance.

2.3.2 Acoustic emission data

To compare the AE activities recorded with different amplifier gains (50 and 60 dB), the gains were corrected to unity (0 dB). The AE events were detected as peaks of the envelope, the amplitudes of which were larger than the threshold. To avoid a possible transient response immediately after the sliding-rate step, we analyzed AE envelopes from 5 to 95% of the sliding distance between consecutive sliding-rate steps. In particular, we counted peaks of the envelope with amplitudes larger than the threshold between 50 and 950 μm of sliding after a sliding-rate step, when the sliding-rate step was imposed after every 1 mm of sliding. As the largest noise level among tests was ~100 μV, the threshold was set to 158 μV, except for the upper sensor of MKB74-4-6a-20221012, wherein the threshold of 251 μV was adopted owing to higher noise levels. As the amplifier for the AE sensor installed in the lower forcing block malfunctioned in MKB74-1-4-20220706, MKB74-4-6a-20220804, MKB74-4-8-20220824, and UFZ-20220927, only the envelopes obtained by the AE sensor installed in the upper forcing block were used for these tests.

If the number of detected AE events is small, the occurrence rate cannot be evaluated correctly. The AE occurrence rates were only evaluated in cases where the number of detected AE events was greater than three. To compare the AE activities at different sliding rates, the AE rate was defined as the number of AE events per unit sliding distance (1 mm). The size distribution provides important information regarding AE activity. However, the number of AE events detected for each steady sliding of the Lamprophyre was less than a few tens. It was difficult to reliably evaluate the size distribution of AE events in these tests. Therefore, only the occurrence rates were used to evaluate the AE activity in this study.

3 Results

The test conditions are listed in Table 1. The obtained initial friction coefficient μ_i and the hardening rate μ_h are shown in Figure 6. To confirm reliability of frictional measurements in this study, the friction coefficients of talc and biotite under ambient conditions and those of quartz under dry, ambient, and wet conditions measured at $\sigma_n =$ 5 MPa using the rotary shear apparatus are shown at the top of Figure 6a. The friction coefficients of talc and biotite are consistent with those obtained by Moore & Lockner (2004) under dry conditions. The friction coefficients of quartz agree well with those measured under various humidities (Frye & Marone, 2002).

The RSF parameters estimated for each sliding-rate step and AE rate for each steady sliding, as well as the friction coefficients, are presented in Supporting Information S1. For simplicity, the rate dependence of steady-state friction ($a - b_1 - b_2$) is denoted as $a - b$. As the estimated values for each sliding-rate step are scattered owing to various factors, including incomplete corrections of the higher-order fluctuation, their averages for every 15 mm of sliding are plotted in Figures 7–12 to show their evolution with respect to the sliding distance. Characteristics of μ_i, μ_h, and RSF parameters for each test condition are described below.

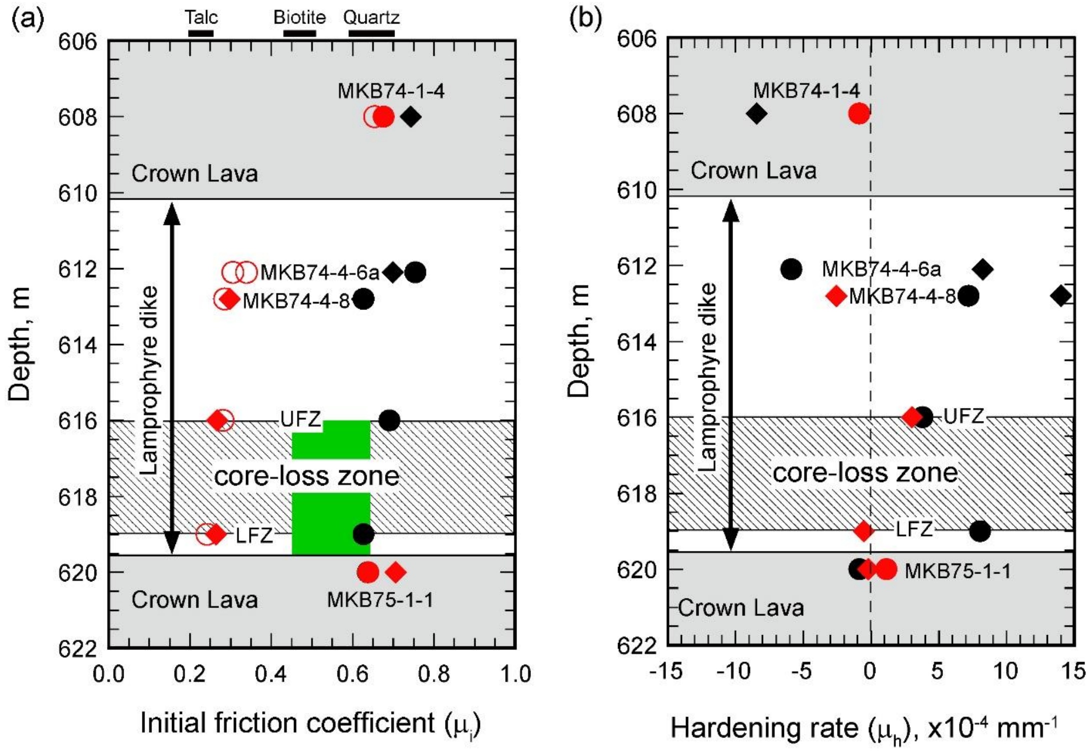

Figure 6. The (**a**) initial friction coefficient μ_i and (**b**) hardening rate μ_h with respect to the depth (distance from the hole collar) along Hole B estimated by fitting equation (1). The estimation errors are smaller than the symbol size. The circle and diamond symbols represent the estimations for tests at σ_n of 15 and 5 MPa, respectively. The black and red colors indicate the dry and wet tests, respectively. Open symbols represent the mean values. The green square in (**a**) at depths from UFZ to below LFZ represents range of friction coefficients measured by Miyamoto et al. (2022) for sliding distances less than 16 mm under room conditions. Ranges of friction coefficients of talc, biotite, and quartz gouges measured by preliminary tests of this study are shown at the top of (**a**) for reference. Friction coefficients of talc and biotite gouges were measured under ambient conditions. Friction coefficients of quartz gouge were measured under dry, ambient, and wet conditions.

Table 1. List of experimental conditions

Test name	Sample	Rock type*	Depth along hole, m	Weight, g	Gouge thickness, mm	Water content, g	Normal stress, MPa	Maximum sliding distance, mm
MKB74-1-4-20220706	MKB74-1-4	CL	608.0	1.00	0.78	Dry	5	172
MKB74-4-6a-20220804	MKB74-4-6a	intact LD	612.1	1.01	0.69	Dry	5	172
MKB74-4-8-20220824	MKB74-4-8	intact LD	612.8	1.01	0.77	Dry	15	172
UFZ-20220927	UFZ	fractured LD	616.0	1.00	0.72	Dry	15	172
LFZ-20220928	LFZ	fractured LD	619.0	1.00	0.75	Dry	15	172
MKB75-1-1-20220929	MKB75-1-1	CL	620.0	1.00	0.82	Dry	15	172
MKB74-1-4-20220930	MKB74-1-4	CL	608.0	1.01	0.86	0.5	15	30**
MKB74-4-6a-20221012	MKB74-4-6a	intact LD	612.1	1.00	0.98	0.5	15	55**
MKB74-4-8-20221118	MKB74-4-8	intact LD	612.8	1.01	0.71	0.2	15	25**
UFZ-20221121	UFZ	fractured LD	616.0	0.99	0.78	0.22	15	115**
LFZ-20221125	LFZ	fractured LD	619.0	0.99	0.63	0.25	15	100**
MKB75-1-1-20221130	MKB75-1-1	CL	620.0	0.98	0.88	0.22	15	172
MKB74-1-4-20221206	MKB74-1-4	CL	608.0	1.00	0.73	0.24	15	172
MKB74-4-6a-20221207	MKB74-4-6a	intact LD	612.1	0.99	0.73	0.25	15	95**
MKB74-4-8-20221209	MKB74-4-8	intact LD	612.8	1.00	0.89	0.23	5	172
UFZ-20221214	UFZ	fractured LD	616.0	0.99	1.12	0.25	5	172
LFZ-20221215	LFZ	fractured LD	619.0	0.99	1.04	0.23	5	172
MKB75-1-1-20221216	MKB75-1-1	CL	620.0	0.99	0.89	0.23	5	172
MKB74-4-6a-20230320	MKB74-4-6a	intact LD	612.1	1.00	0.89	Dry	15	172
MKB74-4-8-20230322	MKB74-4-8	intact LD	612.8	0.99	1.05	Dry	5	172

*: CL and LD represent the Crown Lava and Lamprophyre Dike, respectively.

**: Gouge was squeezed out by this sliding distance. The initial friction coefficient, μ_i, or the hardening rate, μ_h, were not estimated.

3.1. Dry test

The friction coefficients of dry Crown Lava and Lamprophyre were similar. The Lamprophyre samples generally exhibit long-term slip-hardening. The magnitudes and evolution of the RSF parameters and AE activity also depend on the rock type. The RSF parameters of both the Crown Lava and Lamprophyre depend on the applied normal stress, and the normal-stress dependence is more significant in Lamprophyre.

3.1.1 Crown Lava (MKB74-1-4 and MKB75-1-1)

For the Crown Lava sample at $\sigma_n =$ 5 MPa (MKB74-1-4-20220706), $\mu_i =$ 0.743 and $\mu_h = -8.432 \times 10^{-4}$ mm^{-1} (Figure 6), suggesting that the fault is weakened by sliding. At $\sigma_n =$ 15 MPa (MKB75-1-1-20220929), $\mu_i =$ 0.637 and $\mu_h = -0.849 \times 10^{-4}$ mm^{-1}.

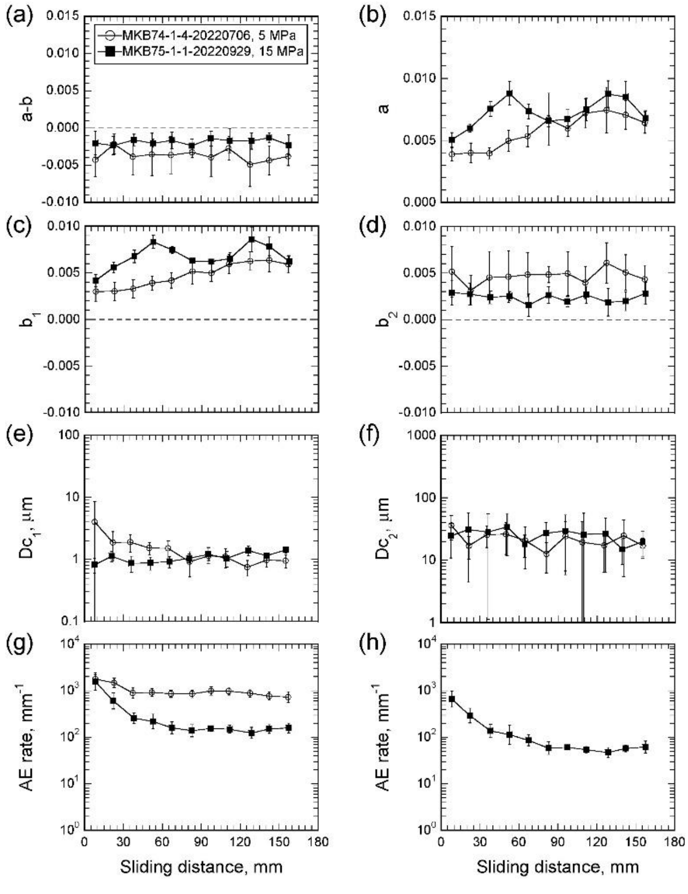

Figure 7. RSF parameters ((**a**) *a*-*b*, (**b**) *a*, (**c**) b_1, (**d**) b_2, (**e**) Dc_1, and (**f**) Dc_2) and AE activities (measured by the (**g**) upper and (**h**) lower sensors) obtained from tests using the dry Crown Lava samples under normal stresses of 5 MPa (open symbols) and 15 MPa (solid symbols).

For both tests, the RSF parameters a and b_1 tend to increase by approximately the same amount with increasing sliding distance (Figures 7b-c). The correlated variations between a and b_1 of MKB75-1-1-20220929 may be caused by a tradeoff in their estimation (Blanpied et al., 1998) and are canceled out in the calculation of $a - b$. Although b_2 is constant and independent of the sliding distance (Figure 7d), it was larger at a lower normal stress. Consequently, $a - b$ at $\sigma_n =$ 5 MPa results in a more negative value (~−0.004) than that for $\sigma_n =$ 15 MPa (~−0.002, Figure 7a). Apart from Dc_1 at $d <$ 15 mm for $\sigma_n =$ 5 MPa, whose standard deviation is significantly large, the shorter (Dc_1) and longer (Dc_2) critical slip distances are 1–2 and 20–30 μm, respectively, regardless of the sliding distance or the normal stress (Figures 7e-f).

The AE activity at $\sigma_n = 5$ MPa that was evaluated using the sensor in the upper forcing block was ~1800 events/mm at the beginning of the test and decreased by approximately half (730 events/mm) with increasing sliding distance (Figure 7g). In the case of $\sigma_n = 15$ MPa (Figures 7g-h), the AE activity reduced more quickly to approximately one-tenth (the upper senser, from ~1600 events/mm to ~160 events/mm; the lower sensor, from ~660 events/mm to ~61 events/mm).

3.1.2 Intact Lamprophyre (MKB74-4-6a and MKB74-4-8)

Two dry and intact Lamprophyre samples were tested under normal stresses of 5 and 15 MPa. The evolution of the RSF parameters and AE activity showed significant normal-stress dependencies.

The initial friction coefficients μ_i were 0.624–0.698 and 0.627–0.754 for σ_n of 5 MPa (MKB74-4-6a-20220804 and MKB74-4-8-20230322) and 15 MPa (MKB-74-4-6a-20230320 and MKB74-4-8-20220824), respectively (Figure 6a). These values are as high as those of dry Crown Lava. The hardening rates μ_h were 8.249–14.020 × 10^{-4} and −5.870–7.187×10^{-4} mm^{-1} for σ_n of 5 and 15 MPa, respectively (Figure 6b). Except for that of MKB-74-4-6a-20230320, the friction of the dry intact Lamprophyre samples exhibited long-term slip hardening.

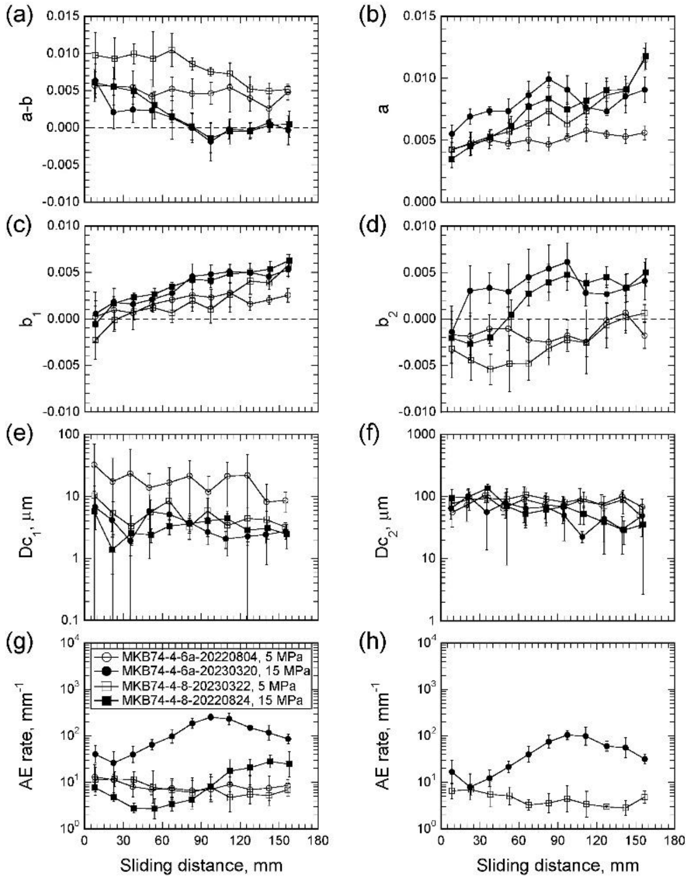

Figure 8. Same as Figure 7 but for the dry intact Lamprophyre samples.

The evolution of RSF parameters at $\sigma_n = 5$ MPa differs slightly between two samples, probably reflecting the initial conditions of gouge layers. For MKB74-4-6a-20220804 (open circles in Figure 8), a was ~0.005 and independent of the sliding distance (Figure 8b), and b_1 increased from 0 to 0.002 (Figure 8c). For MKB74-4-8-20230322 (open squares in Figure 8), a and b_1 increased from 0.004 to 0.01, and −0.002 to 0.005, respectively. For sliding distances of $d < 110$ mm, b_2 values of MKB74-4-6a-20220804 and MKB74-4-8-20230322 were approximately −0.001 and −0.004, respectively, and both of them subsequently increased to ~0 (Figure 8d).

Consequently, the $a-b$ of MKB74-4-6a-20220804 was ~0.005 and was independent of the sliding distance, but decreased from ~0.01 to 0.005 for MKB74-4-8-20230322 with increasing sliding distance (Figure 8a). For both samples, the Dc_1 and Dc_2 values were 10–30 and 70–100 μm, respectively, independent of the sliding distance (Figures 8e-f).

When the intact Lamprophyre samples were tested under $\sigma_n = 15$ MPa (solid symbols in Figure 8), a and b_1 monotonically increased from 0.004 to 0.01 and 0 to 0.006, respectively, with nearly constant rates for both of MKB74-4-6a-20230230 and MKB74-4-8-20220824 (Figures 8b-c). For both the samples, b_2 also increased from −0.002 to 0.004 (Figure 8d). Although the evolution rates of b_2 at $d < 30$ mm differed between the two samples, they were not significant compared with their standard deviations. The evolution of $a-b$ for both samples was similar (Figure 8a). In particular, it decreased from 0.005 to 0 at $d < 90$ mm and was neutral or slightly negative at $d > 90$ mm. The evolutions of Dc_1 and Dc_2 (Figures 8e-f) were similar for the two samples. Although Dc_1 largely deviates, it is almost constant at ~3 μm and slightly shorter than that for $\sigma_n = 5$ MPa. For small sliding distance where b_2 is negative, Dc_2 is 70–100 μm, similar to that for $\sigma_n = 5$ MPa. Subsequently, it decreases (up to 30 μm) after b_2 increases to positive values.

The AE activities measured by the upper sensor under $\sigma_n = 5$ MPa (open symbols in Figure 8g) slightly decrease from a dozen to several events/mm with sliding. The AE activity observed by the lower sensor (Figure 8h) decreased for $d < 150$ mm, but subsequently increased. The AE activity under $\sigma_n = 15$ MPa shows a complicated evolution (solid symbols in Figures 8g-h). In particular, in the case of MKB74-4-6a-20230320, the AE activity measured using the upper AE senser was ~35 events/mm at the beginning of the test and reached its minimum (~20 events/mm) at $d \approx 30$ mm. Subsequently, it increased to ~200 events/mm at $d \approx 90$ mm, followed by a decrease. A similar evolution was observed when the lower AE sensor was used. The AE activity of MKB74-4-8-20220824 was ~8 events/mm at the beginning and reached a minimum of ~3 events/mm at $d \approx 50$ mm. Subsequently, it increased to ~30 events/mm at $d \approx 140$ mm. Although a decrease in the AE rate seems to follow the maximum at $d \approx 140$ mm, it is unclear because the test is terminated at $d = 172$ mm. For both tests at $\sigma_n = 15$ MPa, the sliding distance where the AE rate reached the minimum corresponds to that where b_2 intersects zero from negative to positive values. Although it cannot be clearly recognized owing to low AE activities and the termination of tests just after the b_2 value increased to zero, the same correlation is observed between the evolutions of AE rate and b_2 for the tests at $\sigma_n = 5$ MPa.

3.1.3 Fractured Lamprophyre (UFZ and LFZ)

The evolution of friction and AE activity of two fractured Lamprophyre samples at $\sigma_n = 15$ MPa are identical to those of intact Lamprophyre samples tested under the same normal stress. The initial friction and hardening rate are $\mu_i = 0.627$–0.691 and $\mu_h = 3.814$–8.042×10^{-4} mm^{-1}, respectively (Figure 6). Miyamoto et al. (2022) measured the frictional behaviors of UFZ and Lamprophyre just below the LFZ under ambient conditions using a direct shear apparatus. The friction coefficient at yielding was 0.40–0.45 and increased to 0.65 at $d \approx 16$ mm (green square in Figure 6a). The hardening rate was found to be as high as 0.013–0.016 mm^{-1}, suggesting that the fault properties would evolve rapidly at the beginning of sliding. The friction coefficient at $d = 16$ mm estimated from μ_i and μ_h was 0.64–0.70, consistent with that of 0.65 measured at $d \approx 16$ mm by Miyamoto et al. (2022). The evolution rate may decelerate with sliding and our estimation of μ_h can provide a measure of the terminal evolution-rate.

For both samples, a increased from 0.003–0.004 to 0.01 with increasing sliding distance (Figure 9b). At $d < 100$ mm, b_1 increased from 0.001 to 0.006 and reached a constant value of ~0.006 at $d > 100$ mm (Figure 9c). In the case of UFZ-20220927, b_2 increased from −0.002 to 0.004 at $d < 75$ mm (Figure 9d). For LFZ-20220928, b_2 was −0.001 at the beginning and decreased to −0.004 at $d \approx 45$ mm. Subsequently, it increased to 0.005 at $d \approx 120$ mm. The transition of the b_2 value from negative to positive occurred at $d \approx 30$ and 60 mm for UFZ-20220927 and LFZ-20220928, respectively. In total, the $a - b$ of UFZ20220927 linearly decreased from 0.004 to neutral or slightly negative at $d > 60$ mm (Figure 9a). The $a - b$ value of LFZ-20220928 increased from 0.005 to 0.0065 at $d < 40$ mm. Subsequently, it decreased linearly and became neutral or slightly negative at $d > 90$ mm. Miyamoto et al. (2022) found that the $a - b$ values at $d = 8$–16 mm of UFZ and Lamprophyre just below the LFZ were 0.003 and 0.004, respectively (red square in Figure 9a), which is consistent with that obtained for

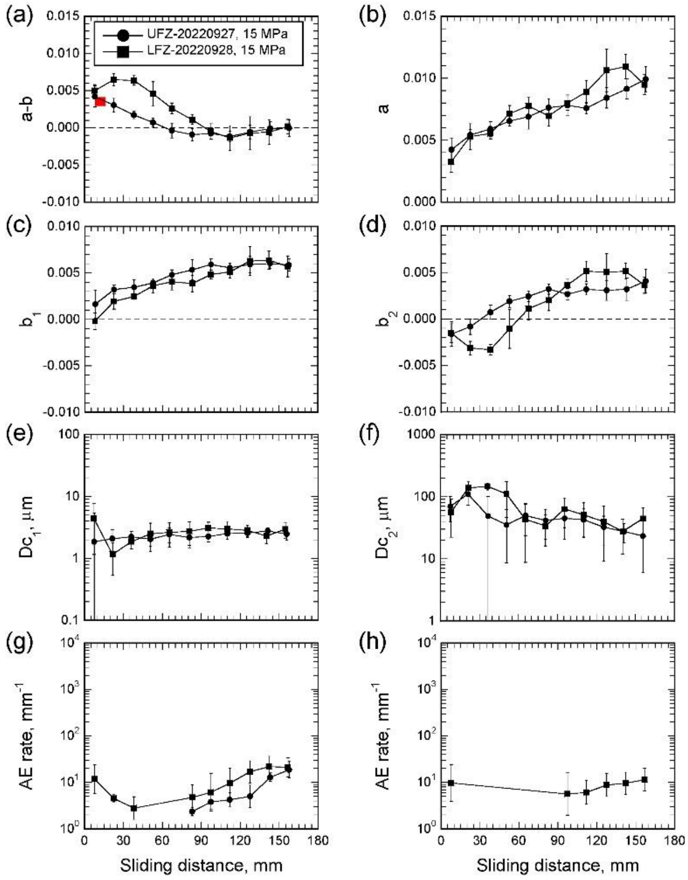

Figure 9. Same as Figure 7 but for the dry fractured Lamprophyre samples. The red square in (**a**) shows the $a - b$ value measured by Miyamoto et al. (2022).

UFZ-20220927 at the corresponding sliding distances in our study. Dc_1 is approximately 2–3 μm for both tests independent of the sliding distance (Figure 9e). Notably, Dc_2 decreased from 100 to 30 μm (Figure 9f), whereas this trend is ambiguous owing to relatively large standard deviations.

In the case of UFZ-20220927, the AE activity was detected only for d > 75 mm (Figure 9g) and increased from 2 to 20 events/mm with increasing sliding distance. An AE activity of ~12 events/mm was detected using the upper AE sensor in LFZ-20220927 at the beginning of the test (Figure 9g). It decreased to ~3 events/mm at $d \approx$ 45 mm. For $45 < d <$ 75 mm, the AE activity was lesser than the detection limit. However, it was detected again at $d \approx$ 75 mm and increased from 5 to 20 events/mm with increasing sliding distance. This suggests that the AE rate of LFZ-20220927 reached a minimum at a sliding distance between 45 and 75 mm, wherein b_2 transitioned from negative to positive at $d \approx 60$ mm. Although the AE rates detected by the lower AE sensor in this test were lower than those detected by the upper AE sensor, a similar evolution was observed (Figure 9h).

3.2 Wet test

Although the friction coefficient of the Crown Lava under wet conditions did not differ from that under dry conditions, the normal-stress dependence of the RSF parameters became more significant. The friction coefficients of the wet Lamprophyre samples were significantly lower than those obtained under dry conditions. Rate-hardening behavior was observed for Lamprophyre samples throughout the tested sliding distance. Notable features of Lamprophyre are the negative b_1 values and occurrence of P-shear. The AE activity of the Crown Lava evolved in a similar manner to that under dry conditions. Although the AE activity of Lamprophyre was low, this implied that its evolution was similar to that under dry conditions.

3.2.1 Crown Lava (MKB74-1-4 and MKB75-1-1)

The friction coefficient and its evolution in the Crown Lava under wet conditions were almost the same as those under dry conditions (Figure 6). Under $\sigma_n =$ 5 MPa (MKB75-1-1-20221216), $\mu_i =$ 0.706 and $\mu_h = -0.205 \times 10^{-4}$ mm^{-1}. At $\sigma_n =$ 15 MPa (MKB75-1-1-20221130 and MKB74-1-4-20221206), $\mu_i =$ 0.639–0.676 and $\mu_h =$ −0.865–1.139 × 10^{-4} mm^{-1}. Neither μ_i nor μ_h of the Crown Lava is affected by water content. In the case of MKB74-1-4-20220930, as the gouge was squeezed out by $d =$ 30 mm, μ_i or μ_h are not estimated, but the mean friction coefficient was found to be 0.673, which is comparable to μ_i under dry conditions at the same normal stress (15 MPa).

Regardless of the normal stress, a and b_1 increase from 0.005 to 0.011 (Figure 10b) and from 0.004 to 0.01 (Figure 10c), respectively. The significant fluctuations in a and b_1 in MKB75-1-1-20221130 may reflect a tradeoff between these parameters. Although the b_2 values for σ_n of 5 and 15 MPa differ by approximately 0.005, they evolve in parallel (Figure 10d). In particular, b_2 decreased by 0.002 for $d < 90$ mm and remained constant (0.006 and 0.001 for σ_n of 5 and 15 MPa, respectively) for $d > 90$ mm. Consequently, the $a - b$ value at $\sigma_n = 5$ MPa increased from −0.01 to −0.005 (Figure 10a). For $\sigma_n = 15$ MPa, the $a - b$ value is less negative than that under $\sigma_n = 5$ MPa and slightly increased from −0.005 to −0.003 with sliding. Thus, the $a - b$ value under wet conditions was more negative by −0.001 than that under dry conditions. Although Dc_1 shows slightly decreasing trends for both tests at σ_n of 5 and 15 MPa, the Dc_1 value depends on the normal stress (Figure 10e). For σ_n of 5 and 15 MPa, the Dc_1 values decreased from 4 to 2 μm and from 2 to 1 μm, respectively. Regardless of the normal stress or the sliding distance, Dc_2 is ~20 μm (Figure 10f).

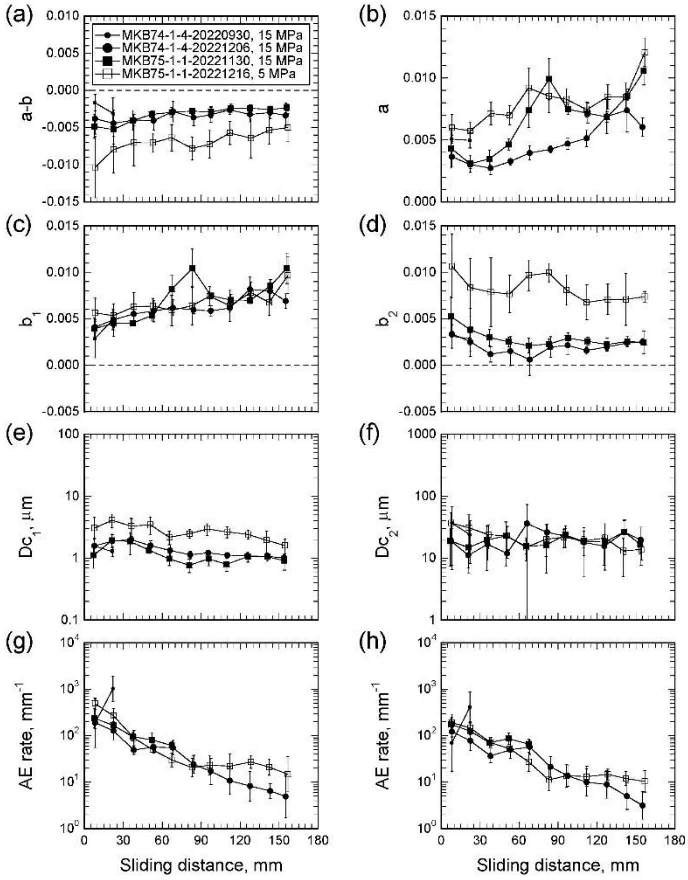

Figure 10. Same as Figure 7 but for the wet Crown Lava samples. A rapid increase in the AE rate of MKB74-1-4-20220930 (small solid circles) may be a result of squeezing out of gouges by a sliding distance of 30 mm, whereas its effect is not significant on the RSF parameters.

For both σ_n of 5 and 15 MPa, the AE activities monotonically decreased from 200–300 to ~10 events/mm with increasing sliding distance (Figures 10g-h).

3.2.2 Intact Lamprophyre (MKB74-4-6a and MKB74-4-8)

At $\sigma_n = 5$ MPa (MKB74-4-8-20221209), $\mu_i = 0.298$ and $\mu_h = -2.555 \times 10^{-4}$ mm^{-1} (Figure 6). As stated earlier, the gouge was squeezed out during three tests under $\sigma_n = 15$ MPa (MKB74-4-6a-20221012, MKB74-4-8-20221118, and MKB74-4-6a-20221207). The initial friction μ_i or the hardening rate μ_h was not estimated. The mean friction coefficients for these tests are 0.282–0.377, similar to μ_i at $\sigma_n = 5$ MPa.

Regardless of the normal stress or the sliding distance, the a and b_1 values are ~0.003 and −0.002–−0.001, respectively (Figures 11b-c). For MKB74-4-8-20221209 ($\sigma_n = 5$ MPa), except for the datum at $d < 15$ mm where the standard deviation is large, b_2 was 0–0.001 (Figure 11d). At $\sigma_n = 15$ MPa, although only the data for $d < 90$ mm are available, b_2 was ~0.002 and independent of the sliding distance. Consequently, the $a - b$ value were ~0.005 and ~0.003 at σ_n of 5 and 15 MPa, respectively. Independent of the normal stress, Dc_1 and Dc_2 values were 5–10 and 70–100 μm, respectively (Figures 11e-f).

The AE activity detected in tests at $\sigma_n = 15$ MPa was less than 10 events/mm at $d < 60$ mm but increased to 100 events/mm at $d > 60$ mm (Figures 11g-h). AE activity was rarely detected for $\sigma_n = 5$ MPa.

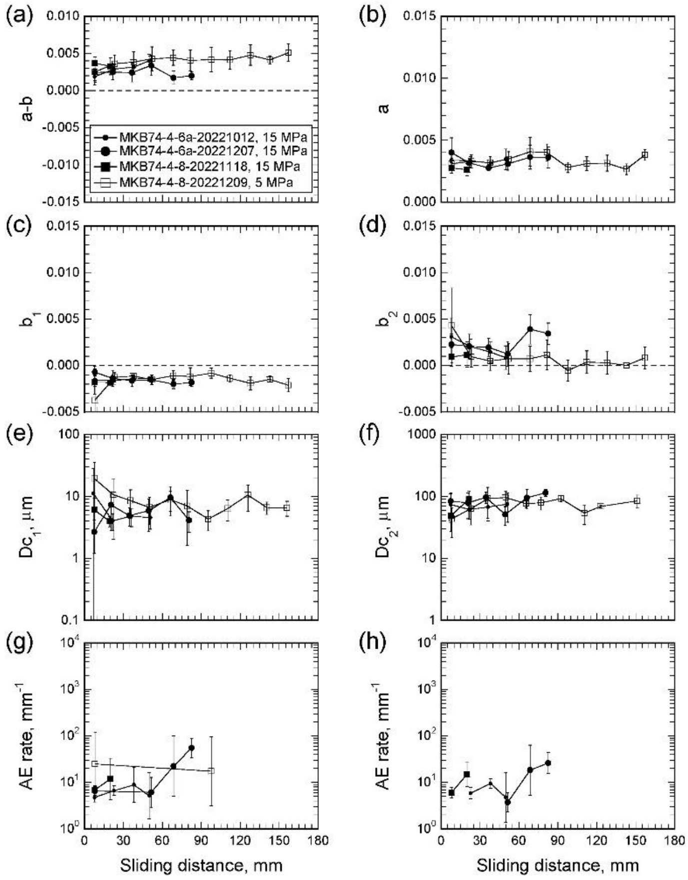

Figure 11. Same as Figure 7 but for the wet intact Lamprophyre samples.

3.2.3 Fractured Lamprophyre (UFZ and LFZ)

When $\sigma_n = 5$ MPa (UFZ-20221214 and LFZ-20221215), $\mu_i = 0.264$–0.267 and $\mu_h = -0.531$–3.016×10^{-4} mm^{-1} (Figure 6). For UFZ-20220927 and LFZ-20220928 at $\sigma_n = 15$ MPa, the gouge was squeezed out during tests. The initial friction or hardening rates were not estimated. The mean friction coefficient for these tests was 0.242–0.281, similar to those at $\sigma_n = 5$ MPa and for the wet and intact Lamprophyre. The wet Lamprophyre was much weaker than the dry Lamprophyre.

Regardless of the normal stress or sliding distance, a was 0.003–0.004 (Figure 12b). Although b_1 or b_2 did not evolve with sliding, they slightly depended on the normal stress (Figures 12c-d). In particular, (b_1, b_2) at $\sigma_n = 5$ MPa is (−0.001, 0–0.001), whereas they are (−0.002, 0.001–0.002) at $\sigma_n = 15$ MPa. The normal stress dependences of b_1 and b_2 are opposite to each other, resulting in $b_1 + b_2 = -0.001$–0 for both normal stresses. Consequently, the $a - b$ value is 0.003–0.004 regardless of the normal stress or sliding distance. For all wet tests of UFZ and LFZ, Dc_1 is constant at 5-10 μm (Figure 12e). At $\sigma_n = 5$ MPa, Dc_2 was 50–70 μm (Figure 12f). It was slightly larger at $\sigma_n = 15$ MPa, at 70–100 μm.

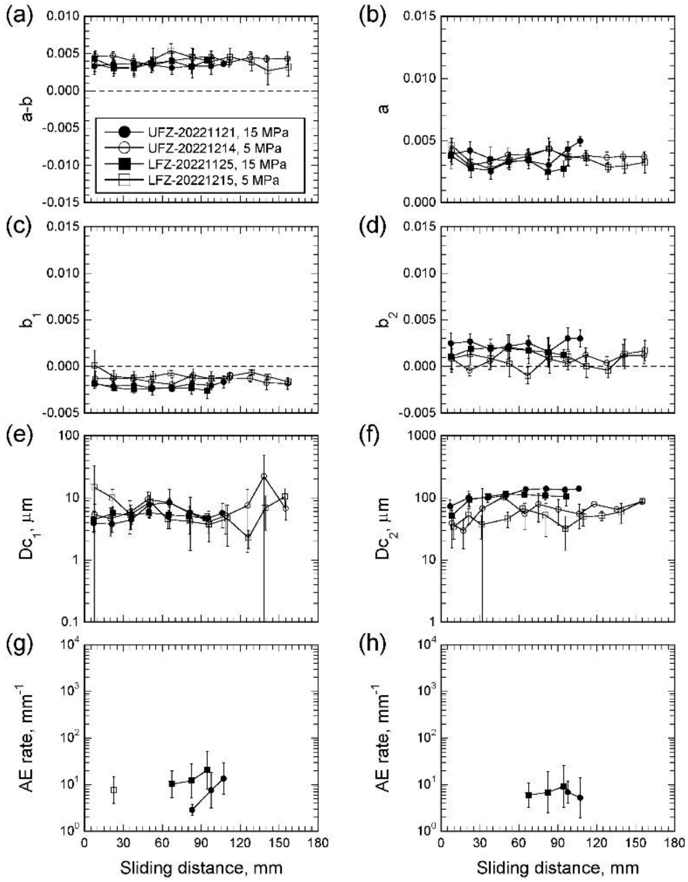

Figure 12. Same as Figure 7 but for the wet fractured Lamprophyre samples.

AE activity is detected only for sliding distances larger than several tens of mm for $\sigma_n = 15$ MPa (Figures 12g-h). This implies that it becomes more active with increasing sliding distance, as was observed for dry Lamprophyre. The AE activity is seldom detected for $\sigma_n = 5$ MPa, suggesting that it depends on the normal stress.

3.3 Texture of gouge layers

Figure 13 shows the gouge layers of dry Lamprophyre after tests at $\sigma_n = 5$ MPa (MKB74-4-8-20230322) and 15 MPa (LFZ-20220928). The granularity of particles in the deformed gouge layer under $\sigma_n = 5$ MPa is similar to that of the particles trapped in the radial groove, which should preserve the initial state. When the interface is opened, the gouge layer is separated along the planes consistent with Riedel (R_1) shear. These results suggest that the shear deformation in the gouge layer has localized to R_1 shears, but that the gouge has not been comminuted considerably and has been loosely packed during sliding at $\sigma_n = 5$ MPa. Conversely, the gouge layer for $\sigma_n = 15$ MPa adheres to the sharp and thin R_1 shears and seems to be well consolidated. The particles in the deformed layer are considerably finer than those trapped in the radial groove, which is consistent with the development of shear bands, wherein larger particles are preferentially comminuted (Marone & Scholz, 1989).

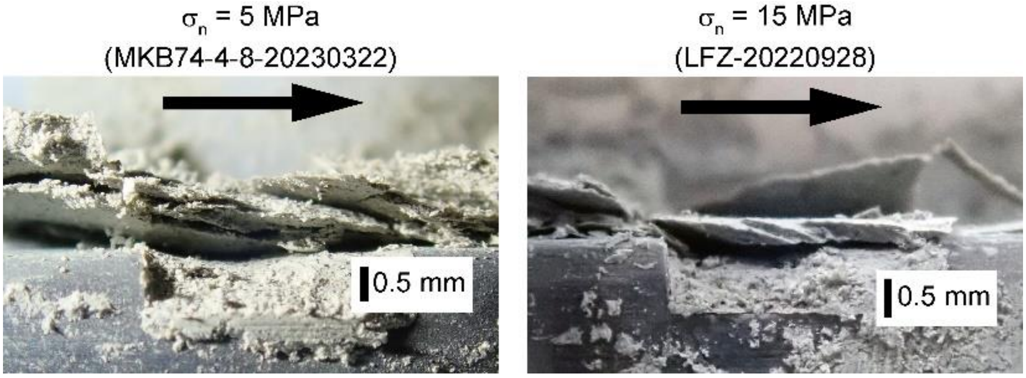

Figure 13. Photographs of the gouge layer of the dry Lamprophyre samples after tests under normal stresses of (**a**) 5 and (**b**) 15 MPa. The black arrow indicates the slip direction of the upper forcing block. The difference in color of gouges in (**a**) and (**b**) is due to differences in lighting conditions.

Figure 14 shows the textures of the gouge layers after the Crown Lava and Lamprophyre tests under dry and wet conditions. Except for the dry Crown Lava (MKB75-1-1-20220929), the applied normal stress was 5 MPa. R_1 shears were developed for the three tests of dry and wet Crown Lava and dry Lamprophyre (Figures 14a-c), wherein a positive b_1 was obtained at the end of the test. In contrast, in the case of the wet Lamprophyre, where b_1 was negative throughout the test, P-shear was produced (Figure 14d).

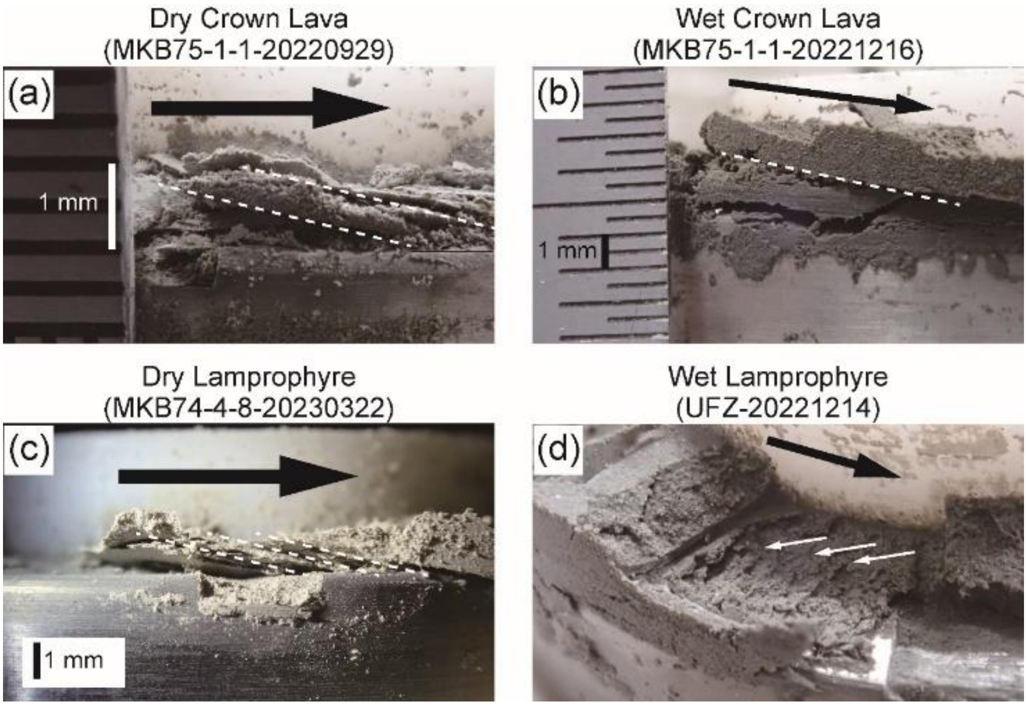

Figure 14. Photographs of the gouge layer after tests of the (**a**) dry Crown Lava (MKB75-1-1-20220929), (**b**) wet Crown Lava (MKB75-1-1-20221216), (**c**) dry Lamprophyre (MKB74-4-8-20230322), and (**d**) wet Lamprophyre (UFZ-20221214). (**c**) The same as Figure 13 (a). The black arrow represents the slip direction of the upper forcing block. The white dashed lines in (**a**)-(**c**) trace shear zones. The white arrows in (**d**) represent the dip of shear zones.

Figure 15 shows the high-resolution X-ray computed tomography (CT) images of the gouge layers parallel to the sliding direction. Although the gouges were carefully collected from the interface, some damage occurred, when the interface was opened (Figure 14). In particular, the gouge layers of the dry Crown Lava ($\sigma_n = 5$ and 15 MPa) and dry Lamprophyre ($\sigma_n = 15$ MPa) were too fragile to recover without serious damage. Therefore, the X-ray CT images of only four cases (wet Crown Lava at $\sigma_n = 5$ and 15 MPa and dry and wet Lamprophyre at $\sigma_n = 5$ MPa) could be captured. In the case of wet Crown Lava at $\sigma_n = 15$ MPa (Figures 15a), R_1 shear is also observed in the X-ray CT image. The transition between R_1 shear and Y-shear is observed in the wet Crown Lava at $\sigma_n = 5$ MPa (Figures 15b). As a complicated fracture network was developed in the dry Lamprophyre at $\sigma_n = 5$ MPa, shear bands cannot be identified. However, the platy minerals are randomly oriented (small white arrows in Figure 15c). In contrast, the platy minerals in the wet Lamprophyre were well oriented along the P-fabric (small white arrows in Figure 15d). As the gouge texture was well-preserved in this case, Y-shear was clearly observed. However, P-shear was not identified, although it is clearly observed in Figure 14d.

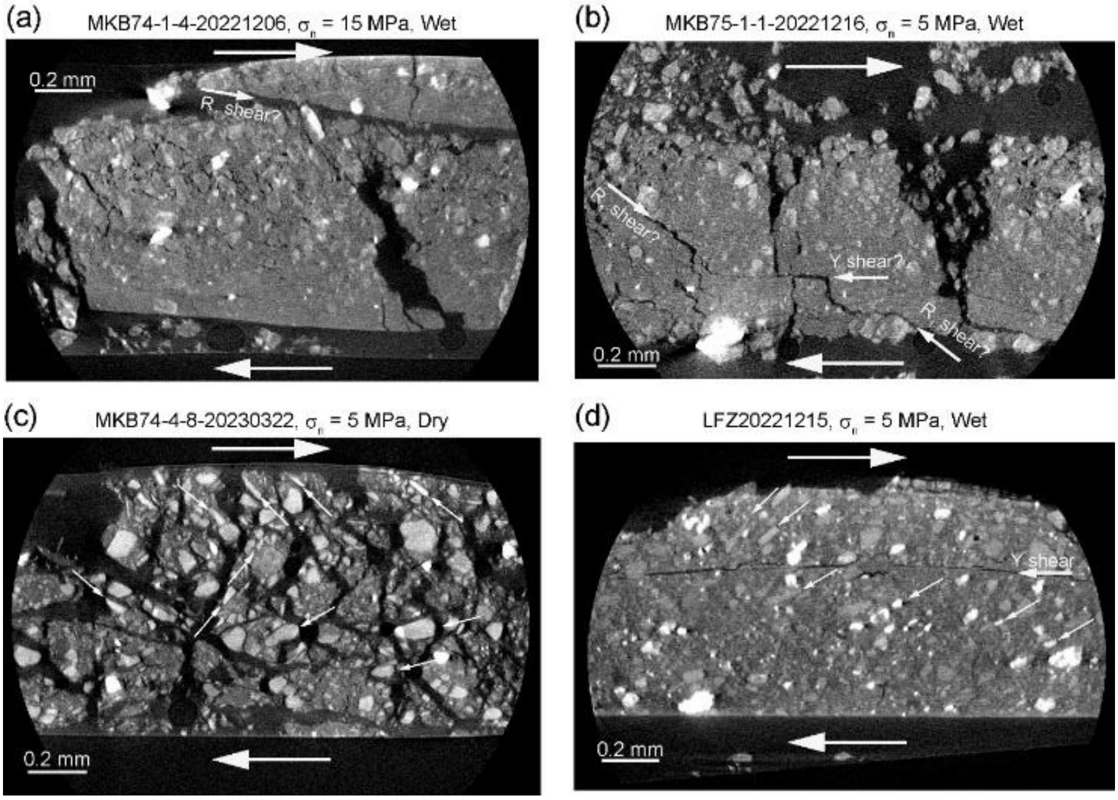

Figure 15. High-resolution X-ray CT images parallel to the sliding direction of gouge layers recovered after the test of **(a)** MKB74-1-4-20221206, **(b)** MKB75-1-1-20221216, **(c)** MKB74-4-8-20230322, and **(d)** LFZ-20221215. The resolution is 1.86 µm. The white arrows at the top and bottom of each panel indicate the sliding direction. Larger white arrows indicate the shear structures of Riedel (R_1) shear or Y-shear. The small white arrows represent the orientations of platy minerals.

4 Discussions

4.1 Relationship between the gouge texture and friction parameters

The evolution of the state variables in the RSF laws reflects the evolution of the real contact area and/or the quality of contact. Variations in b are also interpreted in this context, such as the rate at which the contact area or the quality of the contact recovers. This approach is justified if b is positive. However, although negative b, as in the case of wet Lamprophyre in this study, has often been reported in previous studies (e.g., Belzer & French, 2022; Ikari et al., 2009; Ikari & Saffer, 2011), the underlying physics in view of the contact area has not been elucidated. In contrast, the gouge texture developed during sliding is known to be correlated with the frictional behavior (Bedford & Faulkner, 2021; Beynon & Faulkner, 2020; Moore & Lockner, 2004). Therefore, the variation and evolution of the RSF parameters b_1 and b_2 observed in our study are discussed in terms of the gouge texture.

The X-ray CT images showed that the Crown Lava gouge did not contain platy particles (Figures 15a and b). Therefore, the preferred orientation of shear deformation was not determined by the grain shapes but by the stress state in the gouge layer (Figure 16a). Consequently, R_1 shear should be produced in the Crown Lava regardless of the water content.

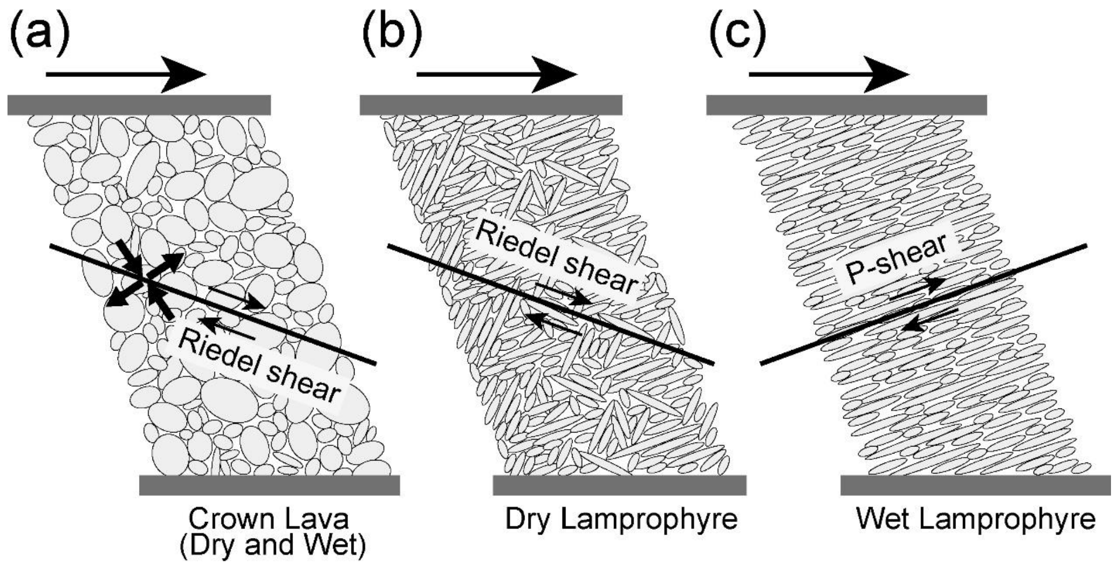

Figure 16. Schematic illustrations of shear band development in the (**a**) dry and wet Crown Lava, and (**b**) dry and (**c**) wet Lamprophyre. The arrow on the top of each model represents the macroscopic sliding direction. The thick arrows in (**a**) show the stress state in the gouge layer. Paired arrows in each model represent the deformation along the shear band in the gouge layer.

For example, Moore & Lockner (2004) and Rutter et al. (1986) observed that platy minerals in clay-rich gouges were aligned with the P-fabric, which is a linearity in the same orientation as P-shear. The former study also reported that the alignment was well-developed in weaker samples. Therefore, the platy particles of sheet minerals (biotite and talc) in the Lamprophyre gouge could be locally aligned when the gouge layer was prepared (Figure 16b). However, in the case of the dry test, the particles should be interlocked by high frictional resistance ($\mu =$ 0.6-0.8), and the development of the preferable alignment through the entire gouge layer can be prevented (Figure 15c). The high friction coefficient of dry Lamprophyre, which is comparable with that in Byerlee's law (Byerlee, 1978), suggests that the shear deformation mechanism may be dominated by processes such as grain fracture rather than interlayer sliding in sheet minerals (Moore & Lockner, 2004; Morrow et al., 2000). Thus, R_1 shear should develop as the preferred shear localization under the stress state in the gouge layer (Moore et al., 1989). As water was added after preparing the gouge layer using the same procedure as that for the dry Lamprophyre, the initial state of particle alignment in wet Lamprophyre should be similar to that in the dry Lamprophyre. When the shear stress is applied, the low friction coefficient of the wet Lamprophyre ($\mu =$ 0.2-0.3) can enable the rotation of platy particles of sheet minerals to ensure that they are normally aligned to the maximum compression in the gouge layer (Figures 15d and 16c). The significant peak in shear stress at the beginning of sliding of the wet Lamprophyre (Supporting Information S1) might represent the work required for the rotation of platy particles. Consequently, P-shear developed along the aligned platy particles over the entire thickness of the gouge layer.

When the gouge layer deformed along the R_1 shear direction, its thickness decreased under constant normal stress. This implies that part of the work required to deform the gouge layer is done by the normal stress and that the gouge layer can deform with less shear stress, resulting in a positive b_1 value, if the sliding-rate step induces a slip along the R_1 shear as a response to a stress rotation in the gouge layer. In contrast, when the gouge layer deformation is localized to P-shear, the shear stress must work against the normal stress to dilate the gouge layer. In this case, b_1 should be negative.

Marone et al. (1992) stated that the frictional property evolves from rate-strengthening to rate-weakening as deformation in the gouge layer evolves from distributed to localized shear. Shear localization is promoted by high normal stress (Bedford & Faulkner, 2021). Therefore, the difference between maturities of R_1 shear under σ_n of 5 and 15 MPa may result in the normal stress-dependent evolution of frictional properties of dry Lamprophyre. The normal-stress dependence of the evolution rate of $a - b$ values was predominantly ascribed to that of b_2. Furthermore, the evolution of b_2 was correlated with that of AE activity. This suggests that brittle processes such as fracturing and comminution of gouge particles to mature shear localization is involved in the evolution of the state variable scaled by b_2 in the RSF law.

4.2 Implication for the 2014 Orkney earthquake

When Hole B intersected the core-loss zone that coincided with the aftershock cloud, drilling water was lost. This suggests that the fault is dry, or that the pore pressure in the fault is less than the water head pressure in the hole (~5 MPa), should it exist. Thus far, as there is no information to determine the case, the implications of laboratory tests in this study for the 2014 Orkney earthquake are discussed for two cases of the dry and wet faults by assuming that the aqueous condition in the fault zone is uniform. The frictional properties of the fault were assumed to be uniform.

4.2.1 In the case of the dry fault

The initial friction μ_i of the Lamprophyre is as large as that of the Crown Lava, and the hardening rate μ_h is higher for the Lamprophyre than for the Crown Lava (Figure 6). Lamprophyre dike may not be the preferred lithology for rupture at the depth drilled by the ICDP-DSeis project. As the normal stress dependence of μ_i for the Crown Lava or Lamprophyre is not significant, we did not expect that the lamprophyre dike might be weaker than the Crown Lava at the nucleation depth (~5 km) of the Orkney earthquake. Therefore, the test results of this study cannot provide a reason for hosting an earthquake in the lamprophyre dike.

Even if the mainshock nucleated at its hypocentral depth, the positive rate-dependence of friction ($a - b > 0$) in the lamprophyre dike may have prohibited its propagation. However, $a - b$ evolves to a negative value as the sliding distance reaches a critical distance, which is shorter under a higher normal stress (Figures 8-9). Therefore, the transition of $a - b$ from positive to negative occurs quickly at large depths, and the rupture can thus propagate. As the rupture propagates to shallower depths, the critical sliding distance increases, and the rupture becomes more difficult to propagate and finally terminates.

Even after the dynamic rupture propagation is terminated, the fractured zone continues to deform to release the stress concentration, resulting in the transition of $a - b$ from positive to negative. The evolution rate of $a - b$ depends on the normal stress, which should be inhomogeneous owing to the heterogeneity of the rock properties and slip on the mainshock fault. The transition of $a - b$ from positive to negative also occurred heterogeneously. Therefore, the distributions of aftershocks in space and size might reflect the inhomogeneity of the normal stress. Furthermore, the stress distribution was disturbed by aftershocks. The aftershock distribution may have evolved in a self-organized manner.

4.2.2 In the case of the wet fault

The friction coefficient of the wet Lamprophyre was considerably lower than those of the dry and wet Crown Lava, regardless of the normal stress (Figure 6a). Lamprophyre dike is preferable for failure. However, the rate-dependence of friction is rate-hardening (Figures 11-12), and does not evolve into rate-weakening. Therefore, additional mechanisms are required to weaken the fault to propagate the mainshock rupture.

The rate-hardening behavior of the wet Lamprophyre is consistent with the termination of mainshock rupture propagation at the depth of ICDP-DSeis drilling, but does not provide a mechanism to host the high aftershock activity. However, the emergence and activation of AE activity with increasing sliding distance (Figures 11-12) would indicate that the instability of the gouge layer on a microscopic scale is enhanced with accumulating deformation. These observations suggest a hierarchical structure of fault properties. Therefore, the coexistence of the termination of mainshock rupture propagation and high aftershock activity in the same fault zone may reflect different layers of the hierarchy of fault properties, which is similar to the relationship between a slow slip event and repeating earthquakes (Ito et al., 2013) or tremors (Obara et al., 2004) in subduction zones.

5 Conclusions

The ICDP-DSeis drilling project successfully recovered rock samples from a fault zone corresponding to the aftershock cloud of the 2014 Orkney earthquake (M5.5) in South Africa. The fault zone occurred in the altered lamprophyre dike hosted by Crown Lava. To elucidate the mechanism underlying the induction of high aftershock activity on the fault where the mainshock rupture terminated, the frictional properties of the Crown Lava and Lamprophyre were measured in the laboratory by imposing sliding-rate steps for large sliding distances of up to 172 mm. The response to the sliding-rate step was modeled using RSF laws with two state variables. We monitored the AE activity associated with the frictional sliding. As drilling water was lost when the borehole reached the fault zone, the laboratory tests were conducted under dry (5% RH) and wet (saturated, but without pore pressure) conditions.

Under the dry condition, the friction coefficients were 0.6–0.8 for both the Crown Lava and Lamprophyre. The rate dependence of steady-state friction $(a - b)$ of the Lamprophyre evolved from positive to negative with increasing sliding distance. The evolution rate was higher under higher normal-stress conditions. The observation of the gouge texture suggests that the normal-stress dependence of the evolution rate should reflect the normal-stress dependence of the comminution and consolidation of gouge particles.

The coefficient of friction of wet Lamprophyre was as low as 0.2–0.3, whereas that of the Crown Lava was independent of the water content. The rate dependence of friction $(a - b)$ of the wet Lamprophyre was positive, independent of the sliding distance, and its RSF parameter was characterized by negative b_1 value in contrast to other tests of the dry and wet Crown Lava and dry Lamprophyre, which showed positive b_1 values. The gouge texture of the wet Lamprophyre was dominated by P-shear, whereas Riedel (R_1) shear developed in other tests. Therefore, the negative b_1 value may be a result of the work done against the normal stress associated with the slip along the P-shear.

Owing to the uncertainty of the aqueous conditions in the fault zone, two cases of implications for the Orkney earthquake were proposed by assuming that the frictional properties and aqueous conditions are uniform along the fault. If the fault zone is dry, although the comparable frictional strength of the Lamprophyre to the Crown Lava cannot explain the selective hosting of the mainshock rupture in the lamprophyre dike, the evolution of the rate dependence of friction can justify the high aftershock activity on the fault that terminates the mainshock rupture propagation. As the evolution of $a - b$ is accelerated under higher normal stress, the spontaneous propagation of the mainshock rupture should be possible at larger depths. Furthermore, the normal-stress dependence of the evolution rate of $a - b$ can explain the spatial and size distributions of the aftershocks.

In the case of a wet fault zone, owing to its weakness, the lamprophyre dike appears to be an optimal site for mainshock rupture. However, as the fault is stable ($a - b > 0$), an additional mechanism is required for spontaneous rupture propagation. Although the $a - b$ value of the wet Lamprophyre is positive regardless of the sliding distance, AE activity emerges and increases with increasing sliding distance. This implies a hierarchical structure for friction. Therefore, the termination of the mainshock rupture and the occurrence of high aftershock activity on the same fault in the lamprophyre dike may reflect frictional properties at different scales or in different layers of a hierarchical fault friction.

Our test results provide a clue for understanding the underlying mechanism of the high aftershock activity in the fault in the lamprophyre dike following the termination of the rupture propagation of the Orkney earthquake. However, these results cannot fully justify the nucleation of the Orkney earthquake in the lamprophyre dike. Drilling to the nucleation depth is required to further elucidate the preparation process of the mainshock.

Acknowledgements

The authors thank Harmony Gold Mining Company Limited for kindly providing access to the research site at the Moab Khotsong mine. The authors also thank B. Liebenberg, all the scientists and operation staff at the ICDP-DSeis Project and ICDP for the drilling site management, downhole logging, and core curation. High-resolution X-ray CT images were obtained under the cooperative research program of the Center for Advanced Marine Core Research (CMCR), Kochi University (Accept Nos. 22A052 and 22B046). This work was supported by JSPS KAKENHI Grant Numbers JP21224012 and JP22K03748, the JSPS-NRF bilateral research project, SATREPS, JSPS Core-to-Core program, the Ministry of Education, Culture, Sports, Science and Technology (MEXT) of Japan, under its Earthquake and Volcano Hazards Observation and Research Program (Earthquake and Volcano Hazard Reduction Research), and the DST-NRF South African Research Chair Initiative (SARChI).

Open Research

The data used in this paper are available at (Yabe et al., 2023).

References

Armstrong, R. A., Compston, W., Retief, E. A., Williams, I. S., &Welke, H. J. (1991). Zircon ion microprobe studies bearing on the age and evolution of the Witwatersrand triad. *Precambrian Research*, 53, 243-266. https://doi.org/10.1016/0301-9268(91)90074-K

Bedford, J. D., & Faulkner, D. R. (2021). The role of grain size and effective normal stress on localization and the frictional stability of simulated quartz gouge. *Geophysical Research Letters*, 48, e2020GL092023. https://doi.org/10.1029/2020GL092023

Belzer, B. D., & French, M. E. (2022). Frictional constitutive behavior of chlorite at low shearing rates and hydrothermal conditions. *Tectonophysics*, 837, 229435. https://doi.org/10.1016/j.tecto.2022.229435

Beynon, S. J., & Faulkner, D. R. (2020). Dry, damp, or drenched? The effect of water saturation on the frictional properties of clay fault gouges. *Journal of Structural Geology*, 140, 104094. https://doi.org/104094. 10.1016/j.jsg.2020.104094

Blanpied, M. L., Marone, C. J., Lockner, D. A., Byerlee, J. D., & King, D. P. (1998). Quantitative measure of the variation in fault rheology due to fluid-rock interactions. *Journal of Geophysical Research*, 103, 9691-9712. https://doi.org/10.1029/98jb00162

Boullier, A. M., Yeh, E. C., Boutareaud, S., Song, S. R., & Tsai, C. H. (2009). Microscale anatomy of the 1999 Chi-Chi earthquake fault zone. *Geochemistry, Geophysics, Geosystems*, 10, Q03016. https://doi.org/10.1029/2008GC002252

Bradbury, K. K., Evans, J. P., Shester, J. S., Chester, F. M., & Kirschner, D. L. (2011). Lithology and internal structure of the San Andreas fault at depth based on characterization of Phase 3 whole-rock core in the San Andreas Fault Observatory at Depth (SAFOD) borehole. *Earth and Planetary Science Letters*, 310, 131-144. https://doi.org/10.1016/j.epsl.2011.07.020

Byerlee, J. (1978). Friction of rocks. *Pure and Applied Geophysics*. 116, 615–626. https://doi.org/10.1007/BF00876528

Carpenter, B. M., Saffer, D. M., & Marone, C. (2015). Frictional properties of the active San Andreas Fault at SAFOD: Implications for fault strength and slip behavior. *J. Geophys. Res. Solid Earth*, 120, 5273–5289. https://doi.org/10.1002/2015JB011963

Chang, T. W., & Ide, S. (2020). Toward comparable relative locations between the mainshock slip and aftershocks via empirical approaches. *Earth, Planets and Space*, 72, 78. https://doi.org/10.1186/s40623-020-01203-4

Chéry, J., Zoback, M., & Hickman, S. (2004). A mechanical model of the San Andreas fault and SAFOD Pilot Hole stress measurements. *Geophysical Research Letters*, 31, L15S13. https://doi.org/10.1029/2004GL019521

Chester, F. M., Rowe, C. Ujiie, K., Kirkpatrick, J. Regalla, C. Remitti, F., Moore, C., Toy, V., Wolfson-Schwer, M., Bose, S., Kameda, J., Mori, J., Brodsky, E., Eguchi, N., Toczko, S., & Expedition 343 and 343T Scientists. (2013). Structure and composition of the plate-boundary slip zone for the 2011 Tohoku-oki earthquake. *Science*, 342, 1208-1211. https://doi.org/10.1126/science.1243719

Dieterich, J. (1979). Modeling of rock friction 1. Experimental results and constitutive equations. *Journal of Geophysical Research*, 84, 2161-2168.

https://doi.org/10.1029/JB084iB05p02161

Fujimoto, K., Ueda, A., Ohtani, T., Takahashi, M., Ito, H., Tanaka, H., & Boullier A. M. (2007). Borehole water and hydrologic model around the Nojima fault, SW Japan. *Tectonophysics*, 443, 174-182. https://doi.org/10.1016/j.tecto.2007.01.015

Fulton, P. M., Brodsky, E. E., Kano, Y., Mori, J., Chester, F., Ishikawa, T., Harris, R. N., Lin, W., Eguchi, N., Toczko, S., Expedition 343, 343T, & KR13-08 Scientists. (2013). Low coseismic friction of the Tohoku-oki fault determined from temperature measurements. *Science*, 342, 1214-1217. https://doi.org/10.1126/science.1243641

ICDP Science Plan 2020-2030. Helmholtz Centre Potsdam, GFZ German Research Centre for Geosciences, Telegrafenberg, D-14473 Potsdam. https://doi.org/10.2312/icdp.2020.001

Ikari, M. J., & Saffer, D. M. (2011). Comparison of frictional strength and velocity dependence between fault zones in the Nankai accretionary complex. *Geochemistry, Geophysics, Geosystems*, 12, Q0AD11. doi:10.1029/2010GC003442

Ikari, M. J., Saffer, D. M., & Marone, C. (2009). Frictional and hydrologic properties of clay-rich fault gouge. *Journal of Geophysical Research*, 114, B05409. http://dx.doi.org/10.1029/2008JB006089

Ito, Y., Hino, R., Kido, M., Fujimoto, H., Osada, Y., Inazu, D., Ohta, Y., Iinuma, T., Ohzono, M., Miura, S., Mishina, M., Suzuki, K., Tsuji, K., & Ashi, J. (2013). Episodic slow slip events in the Japan subduction zone before the 2011 Tohoku-Oki earthquake. *Tectonophysics*, 600,14-26. https://doi.org/10.1016/j.tecto.2012.08.022

Kano, Y., Mori, J., Fujio, R., Ito, H., Yanagidani, T., Nakao, S., & Ma, K. F. (2006). Heat signature on the Chelungpu fault associated with the 1999 Chi-Chi, Taiwan earthquake. *Geophysical Research Letters*, 33, L14306. https://doi.org/10.1029/2006GL026733

Kato, A., & Obara, K. (2014). Step-like migration of early aftershocks following the 2007 Mw 6.7 Noto-Hanto earthquake, Japan. *Geophysical Research Letter*, 41, 3864-3869. https://doi.org/10.1002/2014GL060427

Kim, K. H., Chen, K. C., Wang, J. H., & Chiu, J. M. (2010). Seismogenic structures of the 1999 Mw 7.6 Chi-Chi, Taiwan, earthquake and its aftershocks. *Tectonophysics*, 489, 119-127. https://doi.org/10.1016/j.tecto.2010.04.011

Li, H., Wang, H., Xu, Z., Si, J., Pei, J., Li, T., Huagn, Y., Song, S.-R., Kau, L.-W., Sun Z., Chevalier, M. L., & Liu, D. (2013). Characteristics of the fault-related rocks, fault zones and the principal slip zone in the Wenchuan Earthquake Fault Scientific Drilling Project Hole-1 (WFSD-1). *Tectonophysics*, 584, 23-42. http://dx.doi.org/10.1016/j.tecto.2012.08.021

Ma, K. F., Tanaka, H., Song, S. R., Wang, C. Y., Hung, J. H., Tsai, Y. B., et al. (2006). Slip zone and energetics of a large earthquake from the Taiwan Chelungpu-fault Drilling project. *Nature*, 444(7118), 473-476. https://doi.org/10.1038/nature05253

Manzunzu, B., Midzi, V., Mangongolo, A., & Essrich, F. (2017). The aftershock sequence of the 5 August 2014 Orkney earthquake (ML 5.5), South Africa. *Journal of Seismology*, 21(6), 1323-1334. https://doi.org/10.1007/s10950-017-9667-z

Marone, C., & Scholz, C. (1989). Particle-size distribution and microstructures within simulated fault gouge. *Journal of Structural Geology*, 11, 799-814. https://doi.org/

10.1016/0191-8141(89)90099-0

Marone, C., Hobbs, B. E., & Ord, A. (1992). Coulomb constitutive laws for friction: Contrasts in frictional behavior for distributed and localized shear. *Pure and Applied Geophysics*, 139, 195-214. https://doi.org/10.1007/BF00876327

Midzi, V., Zulu, B., Manzunzu, B., Mulabisana, T., Pule, T., Myendeki, S., & Gubela, W. (2015). Macroseismic survey of the ML5.5, 2014 Orkney earthquake. *Journal of Seismology*, 19(3), 741-751. https://doi.org/10.1007/s10950-015-9491-2

Miyamoto, T., Hirono, T., Yokoyama, Y., Kakenki, S., Yamamoto, Y., Ishikawa, T., Tsuchiyama, A., Katayama, I., Yabe, Y., Ziegler, M., Durrheim, R. J., & Ogasawara, H. (2022). Characteristics of fault rocks within the aftershock cloud of the 2014 Orkney earthquake (M5.5) beneath the Moab Khotsong gold mine, South Africa. *Geophysical Research Letters,* 49, e2022GL098745. https://doi.org/10.1029/2022GL098745

Mogi, K. (1968). Development of aftershock areas of great earthquakes. *Bulletin of Earthquake Research Institute,* University of Tokyo, 46, 175-203.

Moore, D. E. (2014). Comparative mineral chemistry and textures of SAFOD fault gouge and damage-zone rocks. *J. Struct. Geol.*, 68, 82-96. https://doi.org/10.1016/j.jsg.2014.09.002

Moore, D. E., & Lockner, D. A. (2004). Crystallographic controls on the frictional behavior of dry and water-saturated sheet structure minerals. *Journal of Geophysical Research*, 109, B03401. https://doi.org/10.1029/2003JB002582

Moore, D. E., & Rymer, M. J. (2007). Talc-bearing serpentinite and the creeping section of the San Andreas fault. *Nature*, 448, 795-797. https://doi.org/10.1038/nature06064

Moore, D. E., Summers, R., & Byerlee, J. D. (1989). Sliding behavior and deformation textures of heated illite gouge. *Journal of Structural Geology*, 11, 329-342. https://doi.org/10.1016/0191-8141(89)90072-2

Mori, J., Yasutomi, T., Ogasawara, H., Somala, S. N., & Sangaraju, S. (2019). Near-field observations of the rupture for the M5.5 Orkney, South Africa earthquake. Paper presented at Seismological Society of America, 2019 Annual Meeting, Seattle.

Morrow, C. A., Moore, D. E., & Lockner, D. A. (2000). The effect of mineral bond strength and adsorbed water on fault gouge frictional strength. *Geophysical Research Letter*, 27, https://doi.org/815-818. 10.1029/1999GL008401

Nisson, D. M., Kieft, T. L., Drake, H., Warr, O., Sherwood Lollar, B., Ogasawara, H., Perl, S. M., Friefeld, B. M., Gastillo, J., Whitehouse, M. J., Kooijman, E., & Onstott, T. C. (2023). Hydrogeochemical and isotopic signatures elucidate deep subsurface hypersaline brine formation through radiolysis driven water-rock interaction. *Geochimica et Cosmochimica Acta*, 340,65-84. https://doi.org/10.1016/j.gca.2022.11.015

Nkosi, N. Z., Manzi, M. S. D., Westgate, M., Roberts, D., Durrheim, R. J., Ogasawara, H., et al. (2022). Physical property studies to elucidate the source of seismic reflectivity within the ICDP DSeis seismogenic zone: Klerksdorp goldfield, South Africa. *International Journal of Rock Mechanics and Mining Sciences*, 155, 105082. https://doi.org/10.1016/j.ijrmms.2022.105082

Obara, K., Hirose, H., Yamazumi, F., & Kasahara, K. (2004). Episodic slow slip events accompanied by non-volcanic tremors in southwest Japan subduction zone.

Geophysical Research Letters, 31. https://doi:10.1029/2004GL020848.

Ogasawara, H., Durrheim, R. J., Yabe, Y., Ito, T., van Aswegen, G., Grobbelaar, M., et al. (2017). Drilling into seismogenic zones of M2.0–M5.5 earthquakes from deep South African gold mines (DSeis): Establishment of research sites. Paper presented at the ISRM AfriRock—rock mechanics for Africa (ISBN: 978192041995), Cape Town, South Africa.

Ogasawara, H., Liebenberg, B., Rickenbacher, M.　Ziegler, M., van Esterhuizen, H., Onstott, T. C., et al. (2019). 2019 status report: Drilling into seismogenic zones of M2.0–M5.5 earthquakes in South African gold mines (DSeis project). In W. Joughin (Ed.), Deep mining 2019: Proceedings of the ninth international conference on deep and high stress mining (pp. 375-384). The Southern African Institute of Mining and Metallurgy, Johannesburg. https://doi.org/10.36487/ACG_rep/1952_28_Ogasawara

Okubo, M., Cichowicz, A., Ogasawara, H., Murakami, O., & Horiuchi, S.　(2017). Rupture process of the 2014 Orkney earthquake, South Africa. *Journal of Marine Science and Technology*, 17, 75-81. doi:10.15625/1859-3097/17/4b/12995.

Rice, J. (1993). Spatio-temporal complexity of slip on a fault. *Journal of Geophysical Research*, 98, 9885-9907. https://doi.org/10.1029/93JB00191

Ruina, A. (1983). Slip instability and state variable friction laws. *Journal of Geophysical Research*, 88, 10359-10370. https://doi.org/10.1029/JB088iB12p10359

Rutter, E. H., Maddock, R. H., Hall, S. H., & White, S. H. (1986). Comparative microstructures of natural and experimentally produced clay-bearing fault gouges. *Pure and Applied Geophysics*, 124, 3-30. https://doi.org/10.1007/Bf00875717

Schleicher, A. M., Sutherland, R., Townend, J., Toy, V. G., & van der Pluijm, B. A. (2015). Clay mineral formation and fabric development in the DFDP-1B borehole, central Alpine Fault, New Zealand. *New Zealand Journal of Geology and Geophyscs*, 58, 13-21. http://dx.doi.org/10.1080/00288306.2014.979841

Tajima, F. & Kanamori, H. (1985). Global survey of aftershock area expansion patterns. *Physics of the Earth and Planetary Interiors*, 40, 77-137. https://doi.org/10.1016/0031-9201(85)90066-4

Tanikawa, W., Hirono, T., Mukoyoshi, H., Tadai, O., & Lin, W. (2013). Fluid transportation properties in sediments and their role in large slip near the surface of the plate boundary fault in the Japan Trench. *Earth and Planetary Science Letters*, 382, 150-160. http://dx.doi.org/10.1016/j.epsl.2013.08.052

Warr, O., Ballentine, C. J., Onstott, T. C., Nisson, D. M., Kieft, T. L., Hillegonds, D. J., & Sherwood Lollar, B. (2022). ^{86}Kr excess and other noble gases identify a billion-year-old radiogenically-enriched groundwater system. *Nature Communications*, 13, 3768. https://doi.org/10.1038/s41467-022-31412-2

Wu, H. Y., Ma., K. F., Zoback, M., Boness, N., Ito, H., Hung, J. H., & Hickman, S. (2007). Stress orientations of Taiwan Chelungpu-Fault Drilling Project (TCDP) hole-A as observed from geophysical logs. *Geophysical Research Letters*, 34, L01303. https://doi.org/10.1029/2006GL028050

Yabe, Y. (2002). Rate dependence of AE activity during frictional sliding. *Geophysical Research Letters*, 29, 1388. https://doi.org/10.1029/2001GL014369

Yabe, Y., Abe, S., Hofmann, G., Roberts, D., Yilmaz, H., Ogasawara, H., Ito, T., Funato, A., Nakatani, M., Naoi, M., & Durrheim, R. (2022). Stress state in the source region of Mw2.2 earthquake in a deep gold mine in South Africa determined from borehole cores. *Pure and Applied Geophysics*, 179, 1679-1700. https://doi.org/10.1007/s00024-022-02999-w

Yabe, Y., Kato, N., Yamamoto, K., & Hirasawa, T. (2003). Effect of sliding rate on the activity of acoustic emission during stable sliding. *Pure and Applied Geophysics*, 10, 1163-1189. https://doi.org/10.1007/s000240300000

Yabe, Y, Ogasawara, H., & Durrheim, R. (2023). The parameters of RSF law and AE activity for the individual sliding-rate steps [Dataset]. Zenodo. https://doi.org/10.5281/zenodo.10049750

Yabe, Y., Song, S. R., & Wang., C. Y. (2008). In-situ stress at the northern portion of the Chelungpu fault, Taiwan, estimated on boring cores recovered from a 2-km-deep hole of TCDP. *Earth Planets Space*, 60, 809-819. https://doi.org/10.1186/BF03352832

Zoback, M., Hickman, S., Ellsworth, W., & the SAFOD Science Team. (2011). Scientific drilling into the San Andreas Fault Zone—An overview of SAFOD's first five years. *Scientific Drilling*, 11, 14–28. https://doi.org/10.2204/iodp.sd.11.02.2011